# University of Edinburgh

## CLAS Analysis Note

---

# $\mathbb{E}$ Double-Polarization Observable for the Reaction $\gamma n \to K^+\Sigma^-$ from g14 (HDice) Data.

---

J. Fleming, N. Zachariou, D. Watts

October 10, 2017

**Abstract**

This analysis note presents the first measurement of the $\mathbb{E}$ double-polarization observable for the reaction $\gamma n \to K^+ \Sigma^-$ using the polarized hydrogen-deuterium target from the g14 (HDice) run period. Circularly polarized photons of energies between 1.1 and 2.3 GeV incident on the HD-Ice target were used. The analysis note presents the methods used to determine the $K^+ \Sigma^-$ final state and to establish any background processes evident in the yield. The detailed procedure to determine the $\mathbb{E}$ observable is also presented.

# Contents

**4 Results**        36

**5 Discussion and Conclusion**        39

# List of Figures

## List of Tables

# 1 Introduction

This section briefly introduces the reaction of interest and the relevant g14 running conditions as well as the methodology used to experimentally determine the double polarization observable $\mathbb{E}$.

## 1.1 The $\vec{\gamma}\vec{n} \to K^+\Sigma^-$ reaction

Figure 1 shows the reaction $\vec{\gamma}\vec{n} \to K^+\Sigma^-$ on a free neutron target in the center-of-momentum (c.m.) frame. Since free neutron targets do not exist, a deuteron target was used, treating the proton as a spectator. For such a
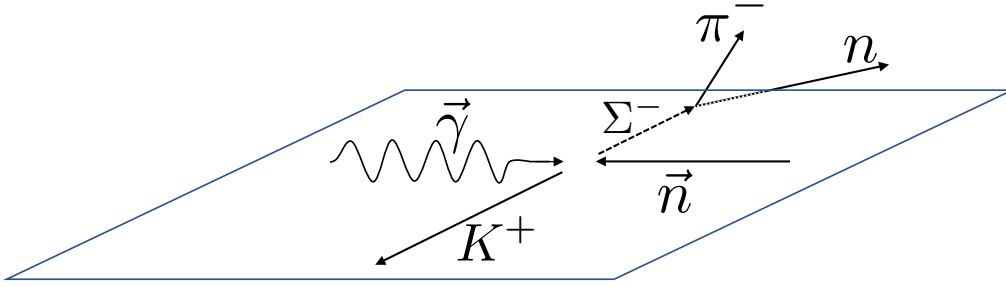


Figure 1: The reaction $\vec{\gamma}\vec{n} \to K^+\Sigma^-$ in the c.m. frame.

"spectator" process the proton recoils with it's initial fermi momentum in deuterium, which is rarely large enough for the proton to reach the CLAS detector. The photoproduced $\Sigma^-$ decays to $n\pi^-$ with a 99.848% branching ratio and $c\tau = 4.434$ cm. The final state of interest can be reconstructed by with the detection of two-charged tracks ($K^+$, and $\pi^-$) and one neutral track in the final state. Due to the limited angular coverage of the Electromagnetic Calorimeter and its low detection efficiency, the reaction is reconstructed with the detection of the two charged tracks only, while assuming the neutron target was at rest. The effect of this assumption on the determination of $\mathbb{E}$ are discussed in Sec. 2.

For photoproduction of scalar mesons from a polarized target with a polarized

photon beam, the differential cross-section is given by [1]:

$$
\begin{aligned}
\frac{d\sigma}{dt} \; = \; & \left(\frac{d\sigma}{dt}\right)_0 [1 - P_{lin}\Sigma\cos(2\phi) \\
& + P_x(-P_{lin}\mathbb{H}\sin(2\phi) + P_\odot\mathbb{F}) \\
& + P_y(\mathbb{T} - P_{lin}\mathbb{P}\cos(2\phi)) \\
& + P_z(P_{lin}\mathbb{G}\sin(2\phi) - P_\odot\mathbb{E})],
\end{aligned}
\tag{1}
$$

where $(P_x, P_y, P_z)$ is the polarization of the target, $P_{lin}$ is the transverse polarization of the beam at an angle $\phi$ to the reaction plane, and $P_\odot$ is the degree of right-circular polarization of the beam. For a longitudinally polarized target and a circularly polarized photon beam Eq. (1) reduces to

$$
\frac{d\sigma}{dt} \; = \; \left(\frac{d\sigma}{dt}\right)_0 [1 - P_z P_\odot \mathbb{E}].
\tag{2}
$$

The methods used to determine the double-polarization observable $\mathbb{E}$ are discussed in Sec. 1.3

## 1.2 The g14 Experiment

### 1.2.1 Running conditions

This analysis used data from the g14 experiment, which run from December 1, 2011 to May 17, 2012 using frozen-spin Hydrogen-Deuteride (HD) targets. The experiment was conducted using circularly and linearly polarized photon beams. For the analysis prescribed here, the circularly polarized data were used, which covered a photon-energy range between 0.6 and 2.5 GeV. The target was longitudinally polarized and data on both orientations were collected. Due to issues outlined in Ref. [2], all upstream and one downstream polarization of the target were not included in this analysis. Table 1.2.1 lists the run period and the corresponding run-conditions **used** in this analysis.

### 1.2.2 The HDice target

The g14 experiment used the HDice target [3], which presented several advantages over other neutron-polarized targets. The HDice target, which can

| Period | Beam Energy (MeV) | Beam Pol (%) | Run Range | Events ($10^6$) | Target Pol (%) |
|---|---|---|---|---|---|
| **Silver 1** | 2280.96 | 81.7 | 68021-68092 | 830 | $+25.6 \pm 0.7$ |
| **Silver 2a** | 2280.96 | 81.7 | 68094-68123 | 393 | $+23.0 \pm 0.6$ |
| **Silver 2b** | 2280.96 | 76.2 | 68124 - 68176 | 777 | $+23.0 \pm 0.6$ |
| **Gold 2a** | 2541.31 | 88.2 | 69227-69254 | 470 | $+26.8 \pm 0.9$ |
| **Gold 2b** | 2541.31 | 83.4 | 69255-69364 | 1626 | $+26.8 \pm 0.9$ |
| **Empty A** | 3355.75 | 82.4 | 68995-69036 | 660 | 0.0 |

Table 1: List of g14 circularly polarized run periods used in this analysis.

achieve high deuteron polarizations ($\sim 25 - 30\%$ with long relaxation times of over one year, has only small contaminations from unpolarized target material, with the main contaminant being the aluminum cooling wires. In addition, its internal NMR system allowed for frequent measurements of the target polarization during the experiment (for more details on NMR measurements see Ref. [4]). Empty target data were collected to subtract contributions from the aluminum cooling wires and the beam entrance and exit windows of the target cell. Details on the empty-target subtraction are presented in Sec. 2. More details on the HDice target and the determination of the deuteron polarization are found in Ref. [2] and references therein.

### 1.2.3 Detector calibration

The calibration of all detector systems used in the g14 run-period were performed using the standard CLAS software packages with some run-specific modifications. These procedures and calibration constants were reviewed and approved by the g14 group and details are outlined in Ref. [2]. The calibration procedure is based on an iterative process since the calibration of various systems is correlated. Because of this, over 12 iterations were performed, following a specific order. Plots that summarize the quality of the calibrations based on reconstructed data on a run-by-run basis are summarized and shown in Ref. [5].

### 1.2.4 Data reconstruction and skimming

The standard CLAS software for data reconstruction (user_ana) was used to "cook" data and translate detector information (TDC and ADC values) to physical information (energies and momenta). The reconstructed particle information was stored in BOS banks and in ROOT trees (using rootbeer ntuples). Several skims were then produced that only kept events that were candidates for the final state of interest, thus reducing significantly the total file size, allowing a faster and easier data analysis. These skims were based on loose momentum-dependent $\beta$ cuts to provide an initial identification of the charged-tracks detected in CLAS. The beta cut range between $\beta^i_{min}$ and $\beta^i_{max}$ was determined as follows:

$$\beta^i_{min/max} = \frac{p}{\sqrt{p^2 + (m^i_{min/max})^2 c^2}} + \alpha^i_{min/max}. \qquad (3)$$

The superscript $i$ in Eq. (3) denotes the particle type (pion, kaon, and proton). The values of the particle mass range $m^i_{min/max}$ and offsets $\alpha^i_{min/max}$ are listed in Table 1.2.4. The analysis outlined in this note used a skim where

| Particle | Momentum Range | Mass Range ($m^i_{min/max}$) | Offsets ($\alpha^i_{min/max}$) |
|---|---|---|---|
| Proton | $0.3 \leq p < 2.5$ GeV | 0.80/1.1 GeV/$c^2$ | -0.06/+0.06 |
| Kaon | $0.2 \leq p < 2.5$ GeV | 0.42/0.6 GeV/$c^2$ | -0.05/+0.05 |
| Pion | $0.1 \leq p < 2.5$ GeV | 0.05/0.3 GeV/$c^2$ | -0.03/+0.03 |

Table 2: Mass and offset parameters used for skimming.

one positive Kaon and one negative pion candidate, with no restrictions on neutral tracks were identified within the $\beta$ limits. These cuts and the further refinements to isolate the $K^+\Sigma^-$ sample are presented in Sec. 2.

### 1.2.5 Energy and momentum corrections

The reconstructed particle momenta extracted using the fitting routines in the user_ana software package give the average particle momenta as measured in the region of the drift-chambers. The particles traversing though the CLAS detector system lose energy through ionization, which should be

accounted for to obtain a more accurate reconstructed momenta for the particle. Furthermore, the reconstructed momenta are based on a magnetic field map calculated in free space, as well as assuming a perfect alignment of the CLAS drift-chamber system, while over time and when placed under field small misalignments of the chambers can arise. These factors contribute to a errors in the reported particle momentum that depends on the particle's position, and momentum. Two sets of corrections were used to improve the determination of the particle momenta: the so-called eloss corrections, as well as momentum corrections. The CLAS eloss package [6], propagates the track from its measured position in drift-chamber layer 1 to its vertex position. The routine assumes a linear path and calculates the energy loss due to ionization in all materials traversed by the track in question.

Momentum corrections functions were identified using kinematic fitting of the high-statistics and kinematically overdetermined reaction $\gamma p \rightarrow p \pi^+ \pi^-$. Details on the kinematic fitting can be found in Ref. [2]. Analysis of this kinematically overdetermined reaction also allowed assessment of the accuracy of the incident photon energy determination. From this analysis small corrections ($< 1\%$) were applied to the photon energies in this analysis (as presented in detail in Ref [2]). The correction for the gravitational sag of the tagging hodoscope (as determined in 2005 from g11 data) was already incorporated in the reconstruction code.

### 1.2.6   Photon beam polarisation

The circularly polarized photon beam was produced via Bremsstrahlung, from a longitudinally polarized electron beam incident on a gold foil. The foil comprised of $10^{-4}$ radiation lengths and was positioned 30 cm upstream of the Hall-B tagger magnet. In the bremsstrahlung process, the electron polarization is transfered to the photons according to [7]:

$$P_\odot = P_{el} \frac{4x - x^2}{4 - 4x + 3x^2}, \text{ with } x = \frac{E\gamma}{E_{el}}, \tag{4}$$

where $P_{el}$ and $E_{el}$ are the electron polarization and energy respectively, and $P_\odot$ is the degree of circular photon polarization. The longitudinal polarization of the electrons was measured throughout the experiment using the Hall-B Møller polarimeter and the energy of the incident beam was given by

the accelerator. The photon energy $E_\gamma$ was measured by the Hall-B Tagger spectrometer on an event-by-event basis. Data with both orientations of the photon circular polarization were collected by flipping the helicity of the incident electron beam pseudo-randomly at about 960 Hz, with the helicity value recorded for each event. More details are given in Ref. [2].

## 1.3 Determination of $\mathbb{E}$

Two methods were employed for the determination of $\mathbb{E}$, both based on the cross-section Eq. (2). In the first method, simple asymmetries were constructed for each kinematic bin, utilizing different orientations of the photon-target polarization. The second approach utilized a maximum likelihood method.

The cross section for each case of photon-helicity and target polarization orientation is (aligned: $\rightrightarrows$; and anti-aligned: $\rightleftarrows$) is given by

$$\frac{d\sigma^{\rightrightarrows}}{dt} = \left(\frac{d\sigma}{dt}\right)_0 [1 - |P_z||P_\odot|\mathbb{E}] \tag{5}$$

$$\frac{d\sigma^{\rightleftarrows}}{dt} = \left(\frac{d\sigma}{dt}\right)_0 [1 + |P_z|, |P_\odot|\mathbb{E}] \tag{6}$$

where $|P_z|$ and $|P_\odot|$ denote the magnitude of the average target and photon polarization respectively. The reaction yield detected, which is proportional to the polarized cross section, incident photon flux, $F^{\rightrightarrows/\rightleftarrows}$, and the detector acceptance, $A(\Omega, p, ...)$, is given by:

$$Y^{\rightrightarrows} \sim F^{\rightrightarrows}[1 - |P_z||P_\odot|\mathbb{E}]A(\Omega, p, ...) \tag{7}$$

$$Y^{\rightleftarrows} \sim F^{\rightleftarrows}[1 + |P_z||P_\odot|\mathbb{E}]A(\Omega, p, ...) \tag{8}$$

### 1.3.1 Method 1:

Assuming $F^{\rightrightarrows} = F^{\rightleftarrows}$, the asymmetry $(Y^{\rightleftarrows} - Y^{\rightrightarrows})/(Y^{\rightleftarrows} + Y^{\rightrightarrows})$ cancels contributions from the detector acceptance and normalization coefficients:

$$\frac{Y^{\rightleftarrows} - Y^{\rightrightarrows}}{Y^{\rightleftarrows} + Y^{\rightrightarrows}} = |P_z||P_\odot|\mathbb{E}. \tag{9}$$

Therefore, the double polarization observable $\mathbb{E}$ can be determined by simple counting statistics in each kinematic bin for aligned and anti-aligned photon-target polarizations:

$$\mathbb{E} = \frac{1}{|P_z||P_\odot|} \frac{Y^{\rightleftarrows} - Y^{\rightrightarrows}}{Y^{\rightleftarrows} + Y^{\rightrightarrows}}. \tag{10}$$

The statistical uncertainty is given by simple error propagation from the uncertainty of the yields ($\sigma_{Y^i} = \sqrt{Y^i}$):

$$\sigma_{\mathbb{E}} = \frac{2}{|P_z||P_\odot|} \sqrt{\frac{Y^{\rightleftarrows} Y^{\rightrightarrows}}{(Y^{\rightleftarrows} + Y^{\rightrightarrows})^3}}. \tag{11}$$

Equation (11) ignores uncertainties in the determination of $|P_z|$ and $|P_\odot|$; these are treated as systematic uncertainties.

### 1.3.2   Method 2:

The second approach uses Eq. (7) and (8) to construct the log-likelihood function:

$$\log L = b + \sum_{i=1}^{Y^{\rightrightarrows}} \log(1 - |P_z^i||P_\odot^i|\mathbb{E}) + \sum_{i=1}^{Y^{\rightleftarrows}} \log(1 + |P_z^i||P_\odot^i|\mathbb{E}), \tag{12}$$

which is maximized using TMinuit [8] to determine the value of $\mathbb{E}$. The constant $b$ in Eq. (12) absorbs the detector acceptance and the normalization coefficients, and has no effect in the maximization of the function as it does not depend on $\mathbb{E}$. The maximization of the log-likelihood function using TMinuit also returns the statistical uncertainty of the determined observable. The value of $\mathbb{E}$, which maximizes the log-likelihood function can be found by taking the first derivative of $\log L$ with respect to $\mathbb{E}$:

$$\frac{\partial \log L}{\partial \mathbb{E}} = -\sum_{i=1}^{Y^{\rightrightarrows}} \frac{|P_z^i||P_\odot^i|}{1 - |P_z^i||P_\odot^i|\mathbb{E}} + \sum_{i=1}^{Y^{\rightleftarrows}} \frac{|P_z^i||P_\odot^i|}{1 + |P_z^i||P_\odot^i|\mathbb{E}}. \tag{13}$$

For illustration purposes, we use the fact that the product $|P_z^i||P_\odot^i|\mathbb{E}$ is much smaller than 0 and expand $\frac{1}{1 \pm |P_z^i||P_\odot^i|\mathbb{E}}$ to the first two terms using a Taylor

expansion $(\frac{1}{1-x} = \sum_{n=0}^{\infty} x^n)$:

$$\frac{\partial \log L}{\partial \mathbb{E}} \approx -\sum_{i=1}^{Y^{\rightrightarrows}} |P_z^i||P_\odot^i|(1 + |P_z^i||P_\odot^i|\mathbb{E}) + \sum_{i=1}^{Y^{\rightleftarrows}} |P_z^i||P_\odot^i|(1 - |P_z^i||P_\odot^i|\mathbb{E}). \quad (14)$$

Setting Eq. (14) to zero and solving for $\mathbb{E}$ we get the value of $\mathbb{E}$ which maximizes our log-likelihood:

$$\hat{\mathbb{E}} = \frac{\sum_{i=1}^{Y^{\rightleftarrows}} |P_z^i||P_\odot^i| - \sum_{i=1}^{Y^{\rightrightarrows}} |P_z^i||P_\odot^i|}{\sum_{i=1}^{Y^{\rightleftarrows}} (|P_z^i||P_\odot^i|)^2 + \sum_{i=1}^{Y^{\rightrightarrows}} (|P_z^i||P_\odot^i|)^2}. \quad (15)$$

It is trivial to show that Eq. (15) reduces to Eq. (10) from Method 1 when $|P_z^i||P_\odot^i| = |P_z||P_\odot|$. The uncertainty of the estimated observable can be determined by taking the inverse of the second derivative with respect to $\mathbb{E}$ evaluated at $\hat{\mathbb{E}}$. For very small values of the product $|P_z^i||P_\odot^i|\mathbb{E}$, the analytical solution illustrated here and numerical solution provide by TMinuit are identical. However, the numerical solution is used as it typically provides a better estimate of the observable.

# 2    Reaction Reconstruction

Skimmed rootbeer ntuples as described in Sec. 1.2.4 were processed for further analysis. This section describes the steps taken to reconstruct the reaction $\gamma n \rightarrow K^+ \Sigma^-$, and the studies performed that estimate background contributions A table that summarizes the cuts applied and their values is given at the end of the section.

## 2.1    Particle identification

The initial particle identification applied on skimming was deliberately quite loose to ensure the yiel of interest was not removed. A more stringent particle ID cut was developed to more reliably identify the final state kaon and pion. For this, two independent measurements were employed to calculate the $\beta$ of each track; one involving information from the Drift Chambers alone (momentum) and one involving information from the TOF system (distance and time). For the former, the charged-track's speed was calculated under assumptions of its mass – that of a pion, and kaon – as follows:

$$\beta^{DC} = \frac{p}{\sqrt{p^2 + (m_{PDG}^i c^2)^2}},\qquad(16)$$

where $m_{PDG}^i$ is the assumed PDG mass for each candidate. Since we are only interested in events with only one $K^+$ and one $\pi^-$ in the final state, positive tracks were assumedto have the mass of the kaon and the negative tracks to have had the mass of a pion. The speed from the TOF system was calculated using the event start time, the time of the hit in the TOF system, and the reconstructed distance traveled by the charged track:

$$\beta^{TOF} = \frac{d^{TOF}}{(t^{TOF} - t^{start})c}.\qquad(17)$$

The two independent measurements of $\beta$ were then compared to each other through $\Delta\beta = \beta^{DC} - \beta^{TOF}$, testing which choice of $m_{PDG}^i$ is correct; for the correct choice, the $\Delta\beta$ momentum dependence lies around 0. Figure 2 shows the $\Delta\beta$ distribution as a function of momentum for the positive (left) and negative (right) track, assuming a kaon and a pion mass respectively. The red lines indicate the nominal particle identification cut applied. Therefore,

a cut on $\Delta\beta$ provided us with the particle identification needed to further process the events of interest. Ideally, as the detector resolution is momentum depended, a momentum-depended $\Delta\beta$ cut is employed. However, we have only seen insignificant effects on the extracted observable from a momentum depended cut, and thus a momentum-independent cut was applied. The effect the particle identification cut has was systematically studied by varying the cut as discussed in Sec. 3.

It is evident from Fig. 2 that a portion of positive pions with high momenta are being misidentified as kaons with this early-stage particle identification cut. Subsequent cuts significantly reduce the misidentified particles (see Sec. 2.3). The vertical lines in the $\Delta\beta$ distribution correspond to particles that originated from other events at adjacent beam-bunches. Such events are removed by our reaction reconstruction cuts described in Sec. 2.4.

## 2.2 Photon selection

Within the timing gate of the tagger focal plane detectors, typically 6 or 7 events are detected in coincidence with the event detected in CLAS (see Fig. 3). Only one of these electrons is associated with the photon initiating the reaction in the target. The other events may be bremsstrahlung electrons associated with photons that did not interact in the target or which were stopped by the collimator or other tagger materials. The correct electron
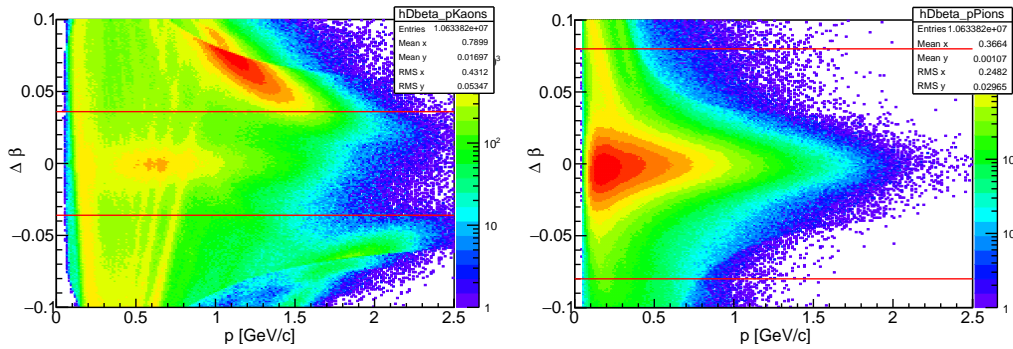


Figure 2: $\Delta\beta$ distribution as a function of momentum for the positive (left) and negative (right) track, assuming a kaon and a pion mass respectively.

10
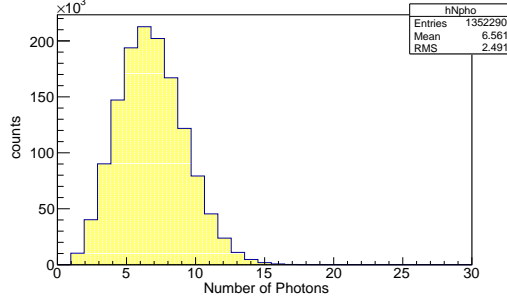
Figure 3: Number of good electron hits in the Tagger Spectrometer for each event.

event is selected from the coincidence time between the detected event in CLAS and the electrons in the tagger focal plane detectors:

$$\Delta t = t_{track} - t_{\gamma}, \tag{18}$$

where $t_{\gamma} = t_{pho} + \frac{7.5 \ cm + z_{vertex}}{c}$, and $t_{track} = t^{TOF} - \frac{d^{TOF}}{\beta^{DC} c}$. The 7.5 cm corresponds to the target offset with respect to the center of the CLAS detector. Figure 4 shows the coincidence time between the focal plane detectors and the kaon (left) or pion (right). The $\sim$ 2 ns beam-bunch structure of the
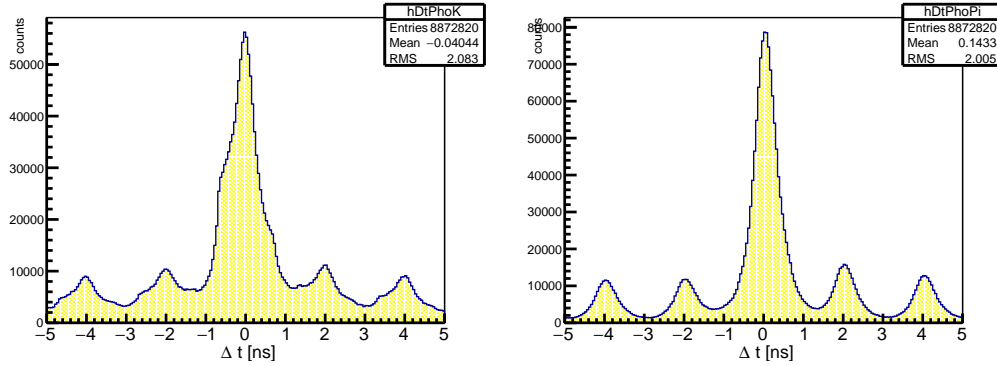


Figure 4: Coincidence time $\Delta t$ between the kaon (left) or pion (right) and all photons with good status registered in the Tagger bank.

accelerator is clearly evident. The electron associated with the photon that initiated the reaction lies within the central beam-bunch centered at 0 ns.

11

The kaon $\Delta t$ shows a less regular structure that results from the inclusion of misidentified pions at this early stage of event selection. With tighter $\Delta\beta$ cuts and event selections subsequently described, the irregular features in the kaon timing are removed. The photon that initiated the reaction is selected as the photon that results in coincidence times between the kaon *and* pion less than 1 ns ($|\Delta t| < 1$ ns). Only events with 1 photon with coincidence times less than $\pm 1$ ns are kept for further analysis.

## 2.3 Particle misidentification

As discussed above and evidenced by Fig. 2 a fraction of positive pions were misidentified as kaons. The majority of these events can be removed using simple cuts on the reaction kinematics to reconstruct the mass of the spectator nucleon. For the reaction of interest $\gamma n \rightarrow K^+\Sigma^-$ the good events will reconstruct to the mass of the nucleon (with Fermi smearing) from the $\Sigma^-$ decay . For misidentified Kaon events then the $\gamma n \rightarrow \pi^+\pi^- X$ reaction (where the misidentified "Kaon" is given the pion mass) would also give a nucleon mass (fermi smeared). The data for these two missing mass calculations is shown as a 2D plot in Fig. 5. The first vertical band at $MM(K^+\pi^-)$ around 0.94 GeV/$c^2$ corresponds to the event of interest. Events with $MM(K^+\pi^-)$ around 0.85 GeV/$c^2$ and $MM(\pi^+\pi^-)$ around 0.95 GeV/$c^2$ correspond to misidentified kaon events. A cut that removes events with $MM(\pi^+\pi^-) < 1.04$ GeV/$c^2$ was applied to reduce misidentified pions.

Figure 6 shows the mass square of the charged tracks

$$m_{calc} = p^2(\frac{1}{\beta^2} - 1.0), \tag{19}$$

before (yellow) and after (blue) the particle-misidentification cut was applied. The top panel shows the positive kaon candidates and the bottom panel the negative pion candidates.

## 2.4 Reaction Reconstruction

The particle-identification, photon-selection, and misidentified-particle cuts select a clean sample of events where the positive charged track corresponds

to a kaon, and the negative to a pion. The reaction was then reconstructed by studying the missing-mass of $\gamma n \to K^+ X$ and $\gamma n \to K^+ \pi^-$ assuming the neutron target at rest. For the reaction of interest we select events where the $MM(\gamma n \to K^+ X))$ correspond to the mass of the $\Sigma^-$ and $MM(\gamma n \to K^+ \pi^-))$ correspond to the mass of the neutron. Figure 7 shows the missing-mass of $\gamma n \to K^+ X$ vs $\gamma n \to K^+ \pi^-$ indicating the different physics channels that contribute. A two-dimensional cut was employed to removed contributions from $\gamma p \to K^+ \Lambda$ and $\gamma p \to K^+ \Sigma^0$ as indicated by the red line in Fig. 7. Events from these reactions that leak above our cut were estimated using simulated data as discussed in the next section. The final cuts that select our reaction of interest are illustrated in Fig. 8. The extent of the cut at higher missing mass was chosen to minimize contributions from the $\Sigma^*$ channels (quantified in Sec. 2.5). Events evident at lower missing mass correspond to events in which the kaon decayed within the CLAS system, which are largely removed by the cut at lower missing masses.

The width of the $\Sigma^-$ peak reflects the detector resolution as well as effects
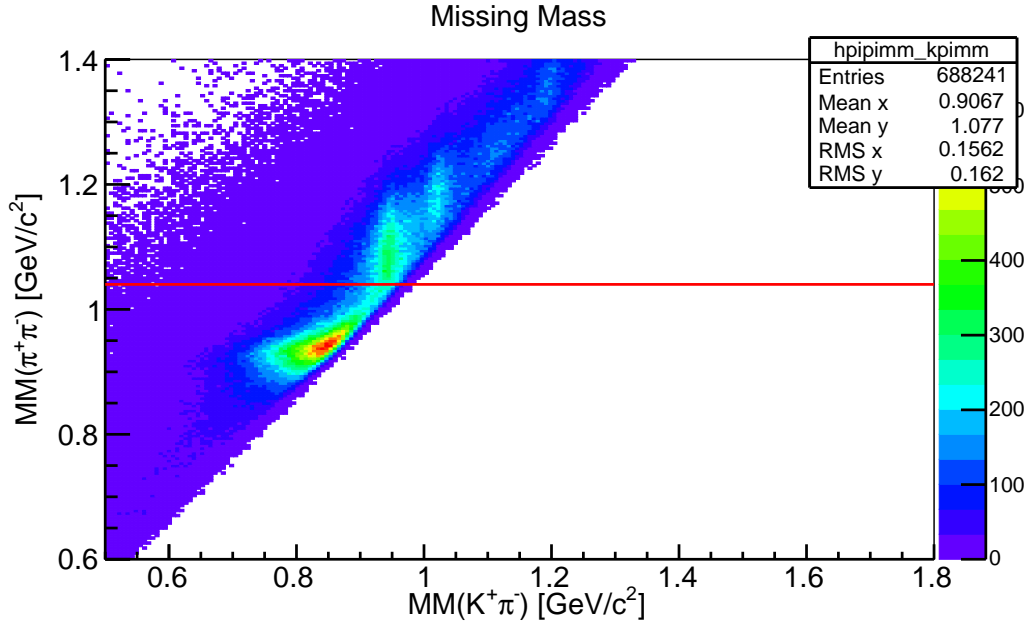


Figure 5: Missing mass of the reaction $\gamma n \to \pi^+ \pi^- X$ (where the identified Kaon is given the pion mass) as a function of $\gamma n \to K^+ \pi^- X$.

13

from assuming that the target neutron at rest. Because of this, a cut on the $MM(\gamma n \to K^+ X)$ reduces contributions from events produced on a target nucleon with high initial fermi momenta. Figure 9 shows the effect that target neutron momentum has on the calculated missing mass $\gamma n \to K^+ X$ using generated data (not processed with GSIM), when assuming the target nucleon is at rest. GSIM processed data, which would reflect the detector resolution further spread the width of the signal. There is a clear correlation between the mass of $\Sigma^-$ and the initial Fermi momentum. This is used to estimate the systematic effect of initial Fermi motion on the extracted values
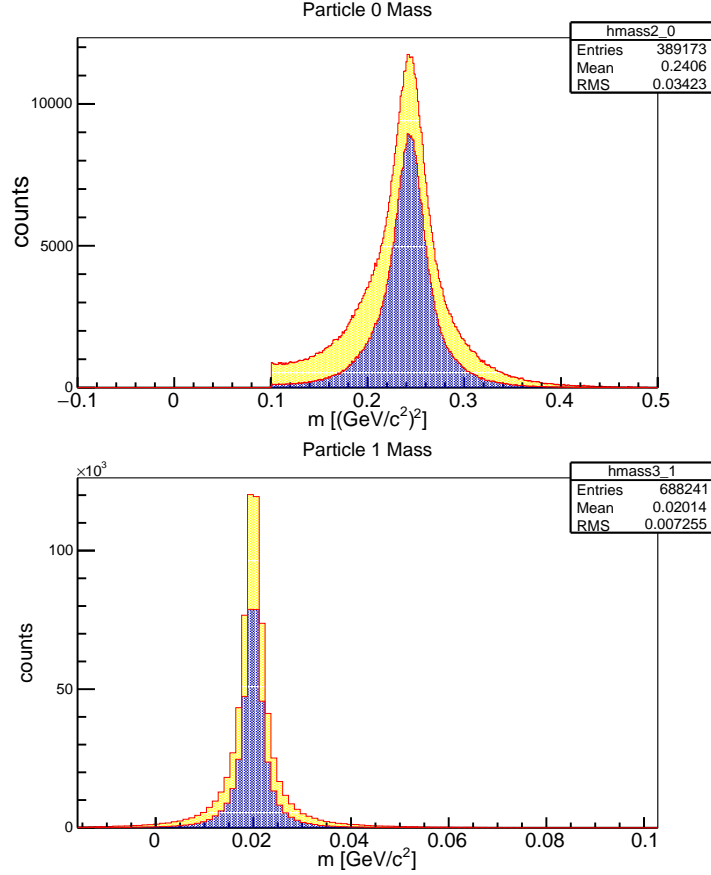


Figure 6: Mass square of the charged tracks calculated before (yellow) and after (blue) the particle-misidentification cut was applied.
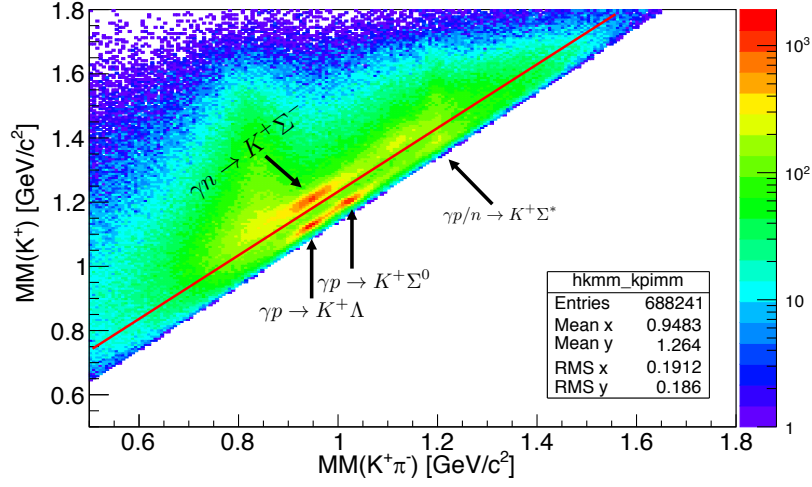
Figure 7: Missing-mass of $\gamma n \to K^+ X$ vs $\gamma n \to K^+ \pi^-$ indicating the different physics channels that contribute.
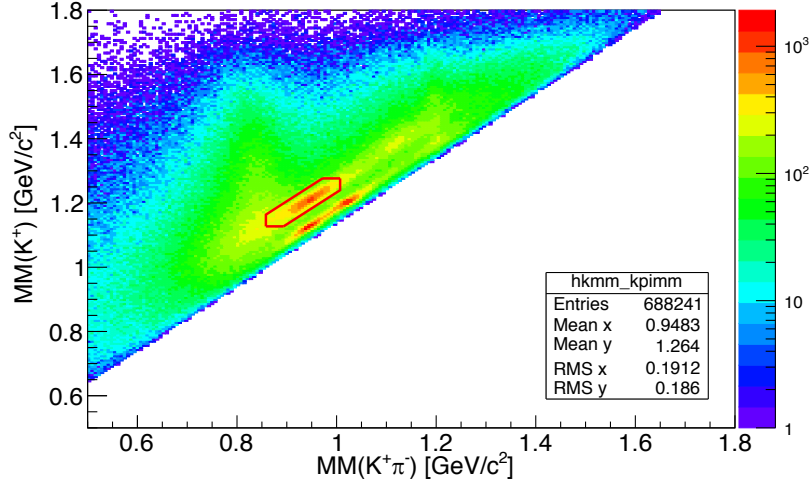


Figure 8: Missing-mass of $\gamma n \to K^+ X$ vs $\gamma n \to K^+ \pi^-$ indicating the sets of cuts that select the reaction of interest.

for E (see Sec. 3) [1].

---

[1]This was done as measuring sufficient experimental quantities to determine the initial Fermi momentum on an event-by-event basis led to unacceptable reduction of the statistical accuracy. Previous work ( see Thesis of J. Fleming [9]) showed the consistency of the
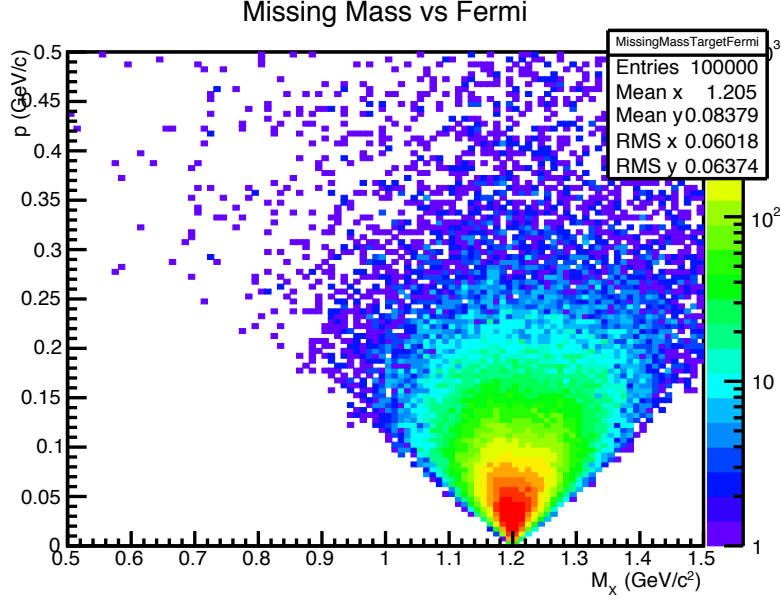
Figure 9: Missing-mass of $\gamma n \rightarrow K^+ X$ as a function of the target nucleon fermi momentum using generated data.

## 2.5 Background studies

As discussed above, background contributions are removed from the data sample by two-dimensional cuts. However, one can argue that a portion of events survives these cuts and contributes to the final data sample used in the determination of $\mathbb{E}$. To establish these contributions, we generated and processed data through a realistic detector simulation (the target nucleons were given a momentum that was sampled from the typical Fermi-momentum distribution). Our nominal cuts were then applied and the remaining contributions from all background channels was investigated. The background channels considered here are (all generated with equal weights)

$$\text{Reaction 1: } \gamma p \rightarrow K^+ \Lambda$$
$$\text{Reaction 2: } \gamma p \rightarrow K^+ \Sigma^0$$
$$\text{Reaction 3: } \gamma n \rightarrow K^+ \Sigma^{*-}$$
$$\text{Reaction 4: } \gamma p \rightarrow K^+ \Sigma^{*0}$$

present results with the event-by-event determination, with limited statistical accuracy.

16

A signal (Reaction 0: $\gamma n \to K^+\Sigma^-$) data sample was also generated. The reconstruction of the GSIM-processed sample was treated the same way as real data, only retaining events where one positive kaon and one negative pion track was reconstructed. Figure 10 shows the distribution of these events (missing-mass of $\gamma n \to K^+ X$ vs missing-mass of $\gamma n \to K^+\pi^- X$) before the application of the reaction reconstruction cuts.
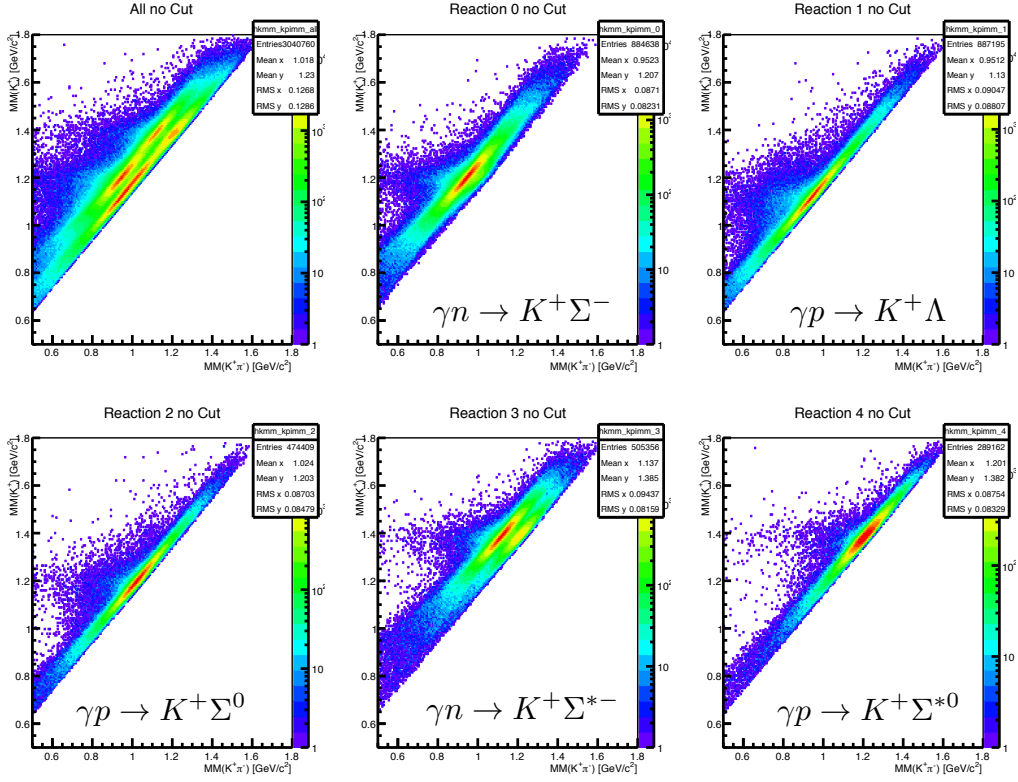


Figure 10: Missing-mass of $\gamma n \to K^+ X$ as a function of the Missing-mass of $\gamma n \to K^+\pi^- X$ for our generated signal sampled (Reaction 0) and background samples (Reactions 1-4), before any reaction reconstruction cuts.

The relative contributions from each reaction channel that survives our re-

17

action identification cuts were:

$$\text{Reaction 0: } 48\%$$
$$\text{Reaction 1: } 0.1\%$$
$$\text{Reaction 2: } 0.2\%$$
$$\text{Reaction 3: } 1.4\%$$
$$\text{Reaction 4: } 0.1\%.$$

The relative contribution is calculated using the ratio of events of the reaction of interest that survive the cuts to the number of events generated for the specific reaction. These findings indicate that a background subtraction is not necessary as the background contributions are sufficiently removed from our data sample with our reaction reconstruction cuts. As cross-sections for background channels are different from the cross section of the reaction of interest, these ratios should be scaled accordingly (the numbers as quoted here are based on the assumption that all reactions have equal production cross sections). For illustration purposes, Fig. 11 shows the missing mass of $\gamma n \rightarrow K^+ X$ from generated data, for our signal events (Reaction 0: blue histogram) and the biggest contribution of background (Reaction 3: red histogram) after reaction reconstruction cuts are applied.

## 2.6   Target-cell contribution

The empty-cell data, listed in Table 1.2.1, were used to account for contributions to the yield of interest yields from the aluminum cooling wires and the beam entrance and exit windows. These contributions come from unpolarized nucleons and thus are associated with $\mathbb{E} = 0$. However, the inclusion of such events dilutes the determined observable. Consider, for example,the yield of events coming from a polarized beam and target:

$$
\begin{aligned}
Y_S^{\rightrightarrows} &= \alpha_S F^{\rightrightarrows}[1 - |P_z||P_\odot|\mathbb{E}_S)]A(\Omega, p, ...) & (20) \\
Y_S^{\rightleftarrows} &= \alpha_S F^{\rightleftarrows}[1 + |P_z||P_\odot|\mathbb{E}_S)]A(\Omega, p, ...), & (21)
\end{aligned}
$$

where $\alpha_S$ is a normalization coefficient accounting for target characteristics, as well as the yield coming from unpolarized events, $Y_B^{\rightrightarrows/\rightleftarrows}$:

$$
Y_B^{\rightrightarrows/\rightleftarrows} = \alpha_B F^{\rightrightarrows/\rightleftarrows}[1 \mp |P_z||P_\odot|\mathbb{E}_B)]A(\Omega, p, ...), \qquad (22)
$$

18
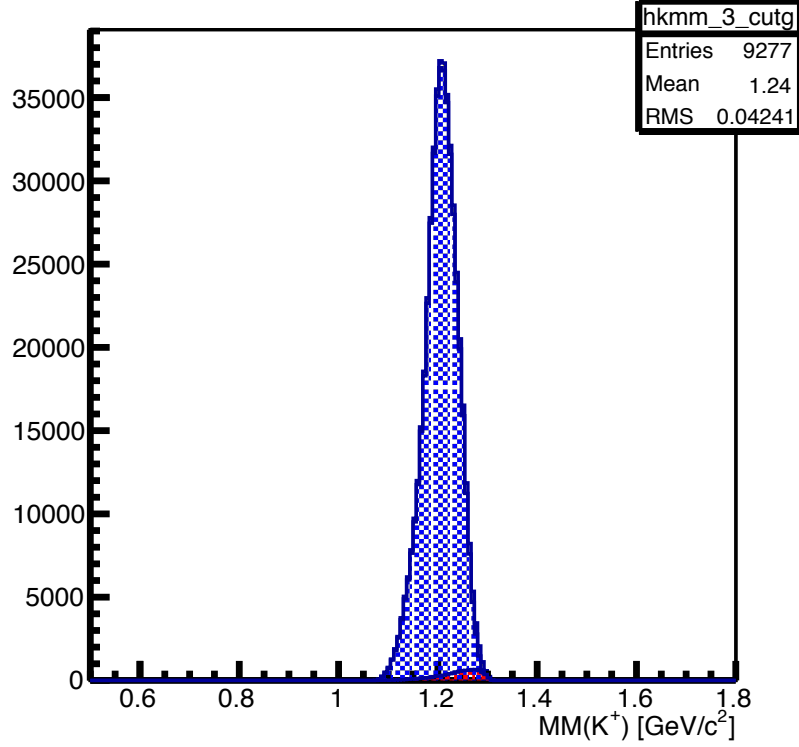
Figure 11: Missing-mass of $\gamma n \to K^+ X$ using generated data for signal reaction (blue histogram) and reaction 3 (red histogram) after all reaction reconstruction cuts.

with $\mathbb{E}_B = 0$. The total yield collected in our data sample is a linear combination of these yields, $Y_S^{\rightrightarrows/\rightleftarrows}$ and a :

$$Y_T^{\rightrightarrows/\rightleftarrows} = Y_S^{\rightrightarrows/\rightleftarrows} + Y_B^{\rightrightarrows/\rightleftarrows}. \tag{23}$$

When the asymmetry is built using $Y_T^{\rightrightarrows/\rightleftarrows}$:

$$\mathcal{A}_{\mathcal{T}} = \frac{Y_T^{\rightleftarrows} - Y_T^{\rightrightarrows}}{Y_T^{\rightleftarrows} + Y_T^{\rightrightarrows}} = \frac{\alpha_S}{\alpha_S + \alpha_B}|P_z||P_\odot|\mathbb{E}_S, \tag{24}$$

and thus

$$\mathbb{E}_S = \frac{1}{d}\frac{1}{|P_z||P_\odot|}\mathcal{A}_{\mathcal{T}}, \tag{25}$$

19

where $d$ is the dilution factor $\frac{\alpha_S}{\alpha_S + \alpha_B}$.

$$
\begin{aligned}
d &= \frac{\alpha_S}{\alpha_S + \alpha_B} \\
&= \frac{\alpha_T - \alpha_B}{\alpha_T} \\
&= 1 - \frac{\alpha_B}{\alpha_T}.
\end{aligned}
\tag{26}
$$

The ratio of $\frac{\alpha_B}{\alpha_T}$ can be calculated by estimating the number of events that originate from the aluminum wires and the entry/exit windows. This is done using empty target data. Specifically, empty-target data are flux-normalized using the In-Beam Cryostat (IBC) located at $z_{vert} \sim 1$ cm (see Fig. refFig:VertexScaled), and the ratio of events (within the target cell $-12 < z_{vert} < -3$ cm) between the flux-normalized empty-target runs and normal production runs gives us $\frac{\alpha_B}{\alpha_T}$. The gold2 run period used a different target cell than the Silver and empty run-periods, and thus a factor that corrects for the relative difference between the gold2 and empty-target target cells is needed. This factor is calculated (see Ref. [2]) to be 0.9. Therefore, the ratio of $\alpha_B$ to $\alpha_T$ is calculated as follows:

1 Flux-normalize empty target data to Silver runs.

2 Obtain $\alpha_B^{silver}$ by integrating between $-12 < z_{vert} < -3$ cm of the flux-normalized empty target data.

3 Flux-normalize empty target data to gold runs.

4 Obtain $\alpha_B^{gold}$ by integrating between $-12 < z_{vert} < -3$ cm of the flux-normalized empty target data.

5 Obtain $\alpha_B = \alpha_B^{silver} + 0.9\alpha_B^{gold}$.

6 Obtain $\alpha_T$ by integrating all production data between $-12 < z_{vert} < -3$ cm.

6 Calculate $\frac{\alpha_B}{\alpha_T}$ and obtain the dilution factor $d$.

Figure 12 shows the reconstructed $z$-vertex position of the kaon for production (yellow) and empty target (blue) runs. The empty target runs were flux-normalized to the gold and silver runs using the IBC data located at $\sim 1$ cm. The red vertical lines show the $z$-vertex cuts applied to select data

20
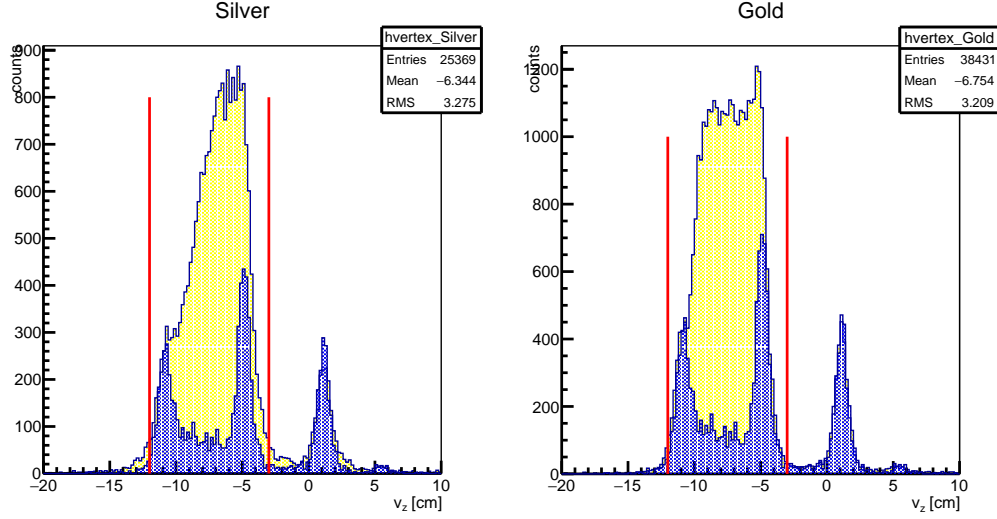
Figure 12: Reconstructed $z$-vertex position of the kaon for production (yellow) and empty target (blue) runs. The red vertical lines show the cuts to select that originate within the target cell.

that originate within the target cell, which are used in the calculation of the dilution factor $d$. The calculated ratio $\frac{\alpha_B}{\alpha_T}$ was found to be equal to 0.2646.

## 2.7   Summary

The reaction reconstruction cuts described in this section allows for a reliable identification of the reaction $\gamma n \to K^+ \Sigma^-$, (relatively) free from background contributions. Table 2.7 summarizes these cuts.

| Cut | Description |
|---|---|
| Particle multiplicity | 1 positive 1 negative |
| Kaon Particle identification | $|\Delta\beta| < 0.036$ |
| Pion Particle identification | $|\Delta\beta| < 0.08$ |
| Photon selection | $|\Delta t| < 1$ ns |
| Photon ambiguity | Events with only 1 $\gamma$ with $|\Delta t| < 1$ ns |
| Particle misidentification | $MM(\gamma n \to \pi^+\pi^- X) > 1.04$ GeV/$c^2$ |
| Production on neutron | 2D cut on $MM(\gamma n \to K^+ X) : y$ as a function of $MM(\gamma n \to K^+\pi^- X) : x$ $0.32 + 0.98 \cdot x > y > 0.25 + 0.98 \cdot x$ |
| $\Sigma^-$ Selection | $0.87 < MM(\gamma n \to K^+\pi^- X) < 1.03$ GeV/$c^2$ $1.15 < MM(\gamma n \to K^+ X) < 1.3$ GeV/$c^2$ |
| $z$-vertex cut | $-12 > z_{vert} > -3$ cm |

Table 3: List of cuts applied to reconstruct the reaction $\gamma n \to K^+\Sigma^-$.

# 3 Systematics Studies

Several sources of systematic uncertainties were investigated. This section lists the ones that had non negligible effect on the determination of the polarization observable. These systematics mainly arise from our cut choices for particle identification, empty target subtraction, and reaction reconstruction, as well as the the uncertainties propagated from the degree of photon polarization.

The estimation of systematic uncertainties that are related with the reaction reconstruction cuts were done by comparing values of the polarization observables between our nominal cuts ($\mathbb{E}_{nom}$) and a tigher or looser cuts ($\mathbb{E}_{tc/lc}$. As these two observables are largely determined from the same data sample, their uncertainties are heavily correlated[2]. The difference $\Delta\mathbb{E} = \mathbb{E}_{nom} - \mathbb{E}_{tc/lc}$ would thus reflect systematic effects as well as statistical fluctuations. To reduce the effect of statistical fluctuations the observable is determined over all $\cos\theta_{c.m.}$ and the difference $\Delta\mathbb{E}$ as a function of $E_\gamma$ is studied. This is justified as no statistically significant systematic dependence on $\cos\theta_{c.m.}$ was found for any of the studies presented in the following sections. For each of these studies, the upper estimate of the systematic uncertainty is taken as the average $\bar{\Delta\mathbb{E}} + RMS_{\Delta\mathbb{E}}$ since also no significant energy dependence in the systematic uncertainty determination is evident. The term $\bar{\Delta\mathbb{E}}$ reflects any systematic offset in the determination, and the term $RMS_{\Delta\mathbb{E}}$ reflects the statistical accuracy of the systematic offset.

## 3.1 Systematic effect of particle identification

### 3.1.1 Kaon PID

The nominal cut for pion identification was varied from $|\Delta\beta| < 0.036$ (which reflects the $3\sigma$ position) to a tighter $|\Delta\beta| < 0.024$ and a looser $|\Delta\beta| < 0.048$ cuts. The biggest effect was seen with the looser cut, with the results and the difference $\Delta\mathbb{E} = \mathbb{E}_{nom} - \mathbb{E}_{lc}$ shown in Fig. 13.

---

[2]As this correlation is unknown the statistical uncertainty was not propagated to the difference $\Delta\mathbb{E}$

Figure 13: Systematic study of Kaon identification. Left panel shows the determined observables for an integrated $\cos\theta_{c.m.}$ bin for two variations of our cut and the right panel shows the difference $\Delta\mathbb{E}$.

From this, an upper value of the systematic uncertainty associated with the Kaon identification cut was estimated at $\sigma^{sys}_{Kaon\ PID} = 0.013$.

### 3.1.2   Pion PID

The nominal cut for Kaon identification was varied from $|\Delta\beta| < 0.08$ to a tighter $|\Delta\beta| < 0.04$. The difference $\Delta\mathbb{E} = \mathbb{E}_{nom} - \mathbb{E}_{lc}$ shown in Fig. 14.

From this, an upper value of the systematic uncertainty associated with the Kaon identification cut was estimated at $\sigma^{sys}_{Pion\ PID} = 0.024$.

## 3.2   Systematic effect of particle misidentification

Misidentified kaon events were removed with a cut on the missing-mass of the reaction $\gamma n \rightarrow \pi^+\pi^- X$ as shown in Fig. 5 ($MM > 1.04$ GeV/$c^2$). A tighter and looser cuts were employed. The biggest difference was seen with a looser cut ($MM > 0.98$ GeV/$c^2$) as shown in Fig. 15.

From this, an upper value of the systematic uncertainty associated with the pion misidentification cut was estimated at $\sigma^{sys}_{Pion\ missPID} = 0.005$.
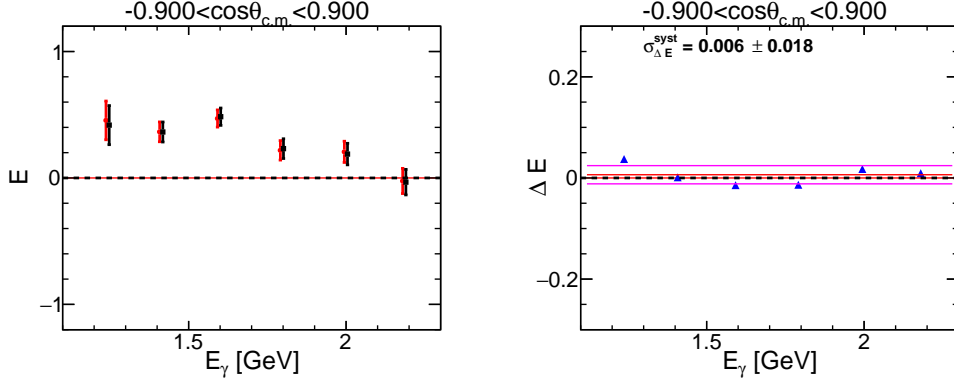
Figure 14: Systematic study of Pion identification. Left panel shows the determined observables for an integrated $\cos\theta_{c.m.}$ bin for two variations of our cut and the right panel shows the difference $\Delta\mathbb{E}$.
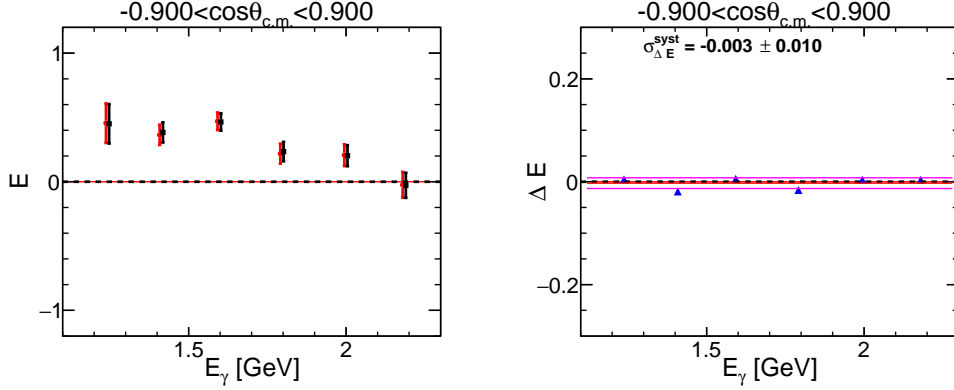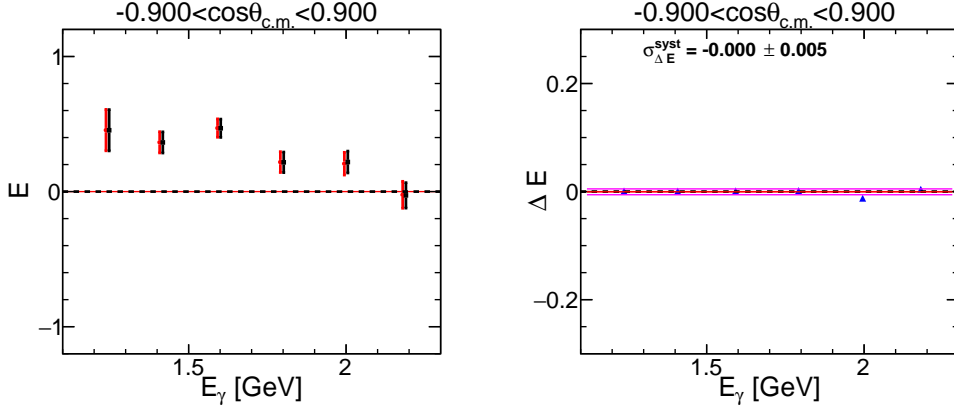


Figure 15: Systematic study of Pion misidentification. Left panel shows the determined observables for an integrated $\cos\theta_{c.m.}$ bin for two variations of our cut and the right panel shows the difference $\Delta\mathbb{E}$.

## 3.3 Systematic effect of $\Lambda/\Sigma^0$ separation

The $\Lambda/\Sigma^0$ event separation was done with the application of a two-dimensional cut as described in Sec. 2.4. The two-dimensional cut was varied to allow more or less $\Lambda/\Sigma^0$ events in our sample, as shown in Fig. 16. This cut provides us with an estimate of the systematic effect from background contributions to our sample. It was discussed in the previous section that the background-
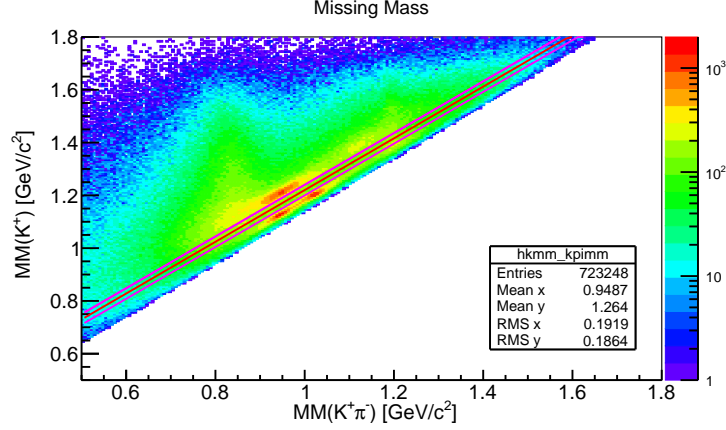
Figure 16: Systematic study of $\Lambda/\Sigma^0$ event separation cut. The red line shows the nominal cut, where the magenta lines shown the looser and tighter cuts.

channel contributions $\gamma p \to K^+\Lambda$, and $\gamma p \to K^+\Sigma^0$ are essentially removed with our nominal cut, as indicated from simulated events. The variation of this cuts provides us with an estimate of $\Lambda/\Sigma^0$-background contributions to our channel. An upper estimate of this systematic is obtained from the difference $\Delta\mathbb{E}$ between the tighter and nominal cuts.

Figure 17 shows the determined observable and the difference between the nominal and a tighter cut. From this, an upper value of the systematic uncertainty associated with this cut was estimated at $\sigma^{sys}_{\Lambda/\Sigma^0\ sep} = 0.055$.

## 3.4 Systematic effect of Kaon-decayed events

Kaons could decay within the CLAS detector resulting in deviations to their determined momenta. These events cause the vertical structure seen in Fig. 16 right below the events of interest. Contributions from these events were effectively reduced by three cuts: one that is parallel to the $\Lambda/\Sigma^0$ separation cut, a cut on the $MM_{\gamma n \to K^+\pi^- X}$, and a cut the $MM_{\gamma n \to K^+ X}$. Figure 18 shows the nominal cuts applied along with their variations to study the systematic effect of decayed kaon contributions.

Figure 19 shows the determined observable and the difference between the

26

nominal and the tighter cut. From this, an upper value of the systematic uncertainty associated with this cut was estimated at $\sigma^{sys}_{Kaon\ decay} = 0.048$.



Figure 17: Systematic study of $\Lambda/\Sigma^0$ event contribution to our sample. Left panel shows the determined observables for an integrated $\cos\theta_{c.m.}$ bin for two variations of our cut and the right panel shows the difference $\Delta\mathbb{E}$.
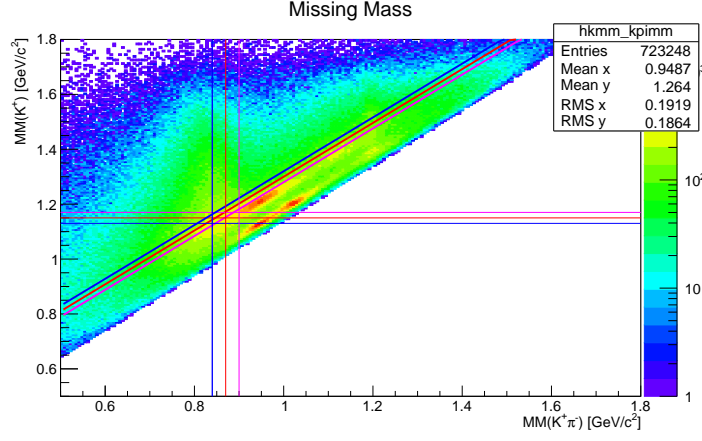
Figure 18: Cuts employed to remove kaons that decay within the CLAS system. The red lines shows the nominal cuts, the magenta lines shown the tighter cuts, and the blue lines show the looser cuts. All other cuts were applied at their nominal positions.
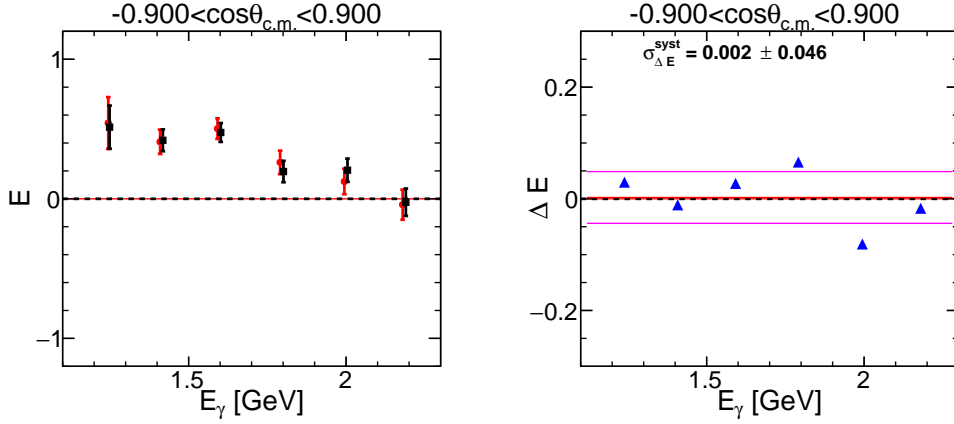


Figure 19: Systematic study of contributions from kaons that decay within CLAS. Left panel shows the determined observables for an integrated $\cos\theta_{c.m.}$ bin for two variations of our cut and the right panel shows the difference $\Delta\mathbb{E}$.

## 3.5   Systematic effect of $\Sigma^*$ separation

As discussed in the previous section, the biggest background contribution to our events resulted from the reactions $\gamma n \rightarrow K^+\Sigma^{*-}$ and $\gamma p \rightarrow K^+\Sigma^{*0}$. Our

simulation studies indicated that these contributions do not exceed 2% with our reaction reconstruction cuts. To estimate further any contributions from these channels, we varied a set of two cuts: a cut on the $MM_{\gamma n \to K^+ \pi^- X}$, and a cut the $MM_{\gamma n \to K^+ X}$ as indicated by Fig. 20.
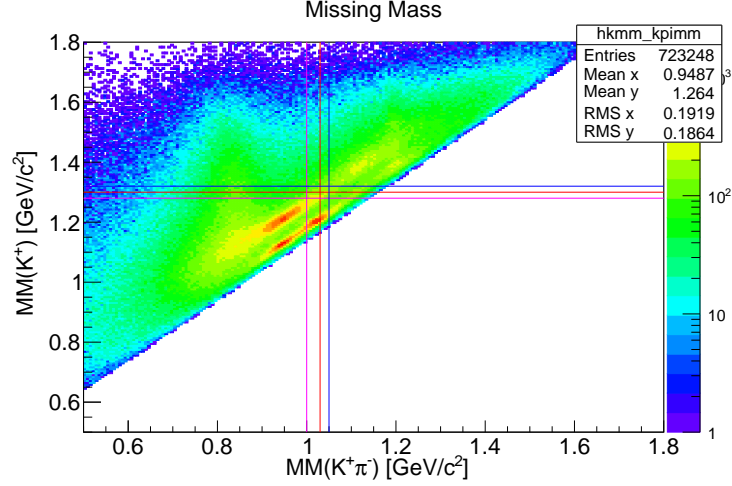


Figure 20: Cuts employed to remove contributions from $\gamma n \to K^+ \Sigma^{*-}$ and $\gamma p \to K^+ \Sigma^{*0}$ reactions. The red linea shows the nominal cuts, the magenta lines shown the tighter cuts, and the blue lines show the looser cuts. All other cuts were applied at their nominal positions.

Figure 21 shows the determined observable and the difference between the nominal and the tighter cut. From this, an upper value of the systematic uncertainty associated with this cut was estimated at $\sigma_{\Sigma^*}^{sys} = 0.047$.
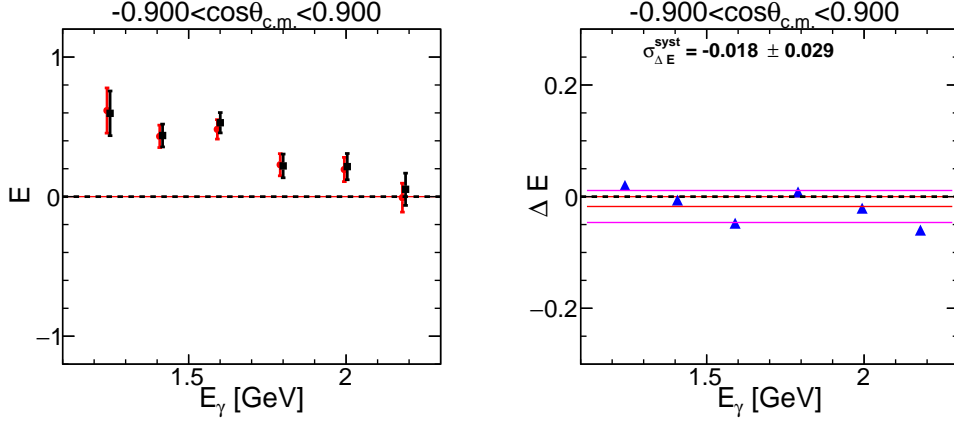
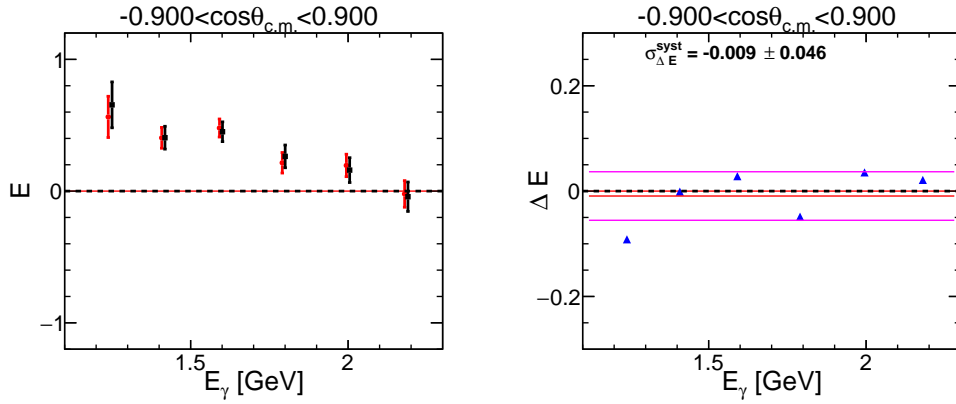Figure 21: Systematic study of contributions from kaons that decay within CLAS. Left panel shows the determined observables for an integrated $\cos\theta_{c.m.}$ bin for two variations of our cut and the right panel shows the difference $\Delta\mathbb{E}$.

## 3.6 Systematic effect of empty target subtraction

The empty target subtraction procedure followed here is based on two assumptions: a) the empty target data and polarized target data are properly flux-normalized and b) the empty target data are associated with $\mathbb{E} = 0.0$. The latter assumption was checked by determining the asymmetry $(Y^{\rightleftarrows} - Y^{\rightrightarrows})/(Y^{\rightleftarrows} + Y^{\rightrightarrows})$ for empty-target data as shown in Fig. 22. It is evident that the asymmetry of empty target data is zero consistent with our assumption.

As discussed in the previous section, the empty-target data are flux-normalized using the IBC, which contains a fixed Kel-F cap downstream of the target cell. The scaling of the empty target data to the polarized target data is thus associated with a statistical uncertainty that should be propagated to the dilution factor $d$. Furthermore, the ratio $\alpha_B/\alpha_T$ is also associated with a statistical uncertainty, as is calculated using integrated yields within the target cell of scaled empty target data and production data. The effect of these sources can be estimated by varying the value of the ratio $\alpha_B/\alpha_T$. As the uncertainty of this ratio depends on statistics, we take as an upper estimate of the standard deviation of $\alpha_B/\alpha_T$ to be twice the statistical uncertainty of the asymmetry $(Y^{\rightleftarrows} - Y^{\rightrightarrows})/(Y^{\rightleftarrows} + Y^{\rightrightarrows})$. Then for each kinematic bin $\alpha_B/\alpha_T$
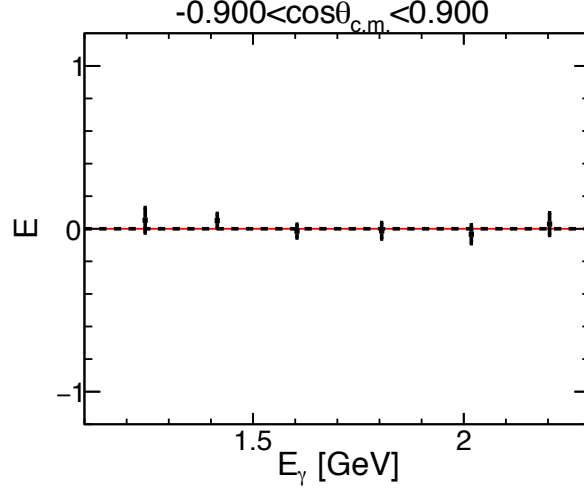
Figure 22: Asymmetry $(Y^{\rightleftarrows} - Y^{\rightrightarrows})/(Y^{\rightleftarrows} + Y^{\rightrightarrows})$ of empty target data.

is randomly chosen from a Gaussian distribution with mean the calculated value of $(\alpha_B/\alpha_T)_{calc}$ and a standard deviation equal to twice the statistical uncertainty of the asymmetry. Then the observable $\mathbb{E}$ is calculated following Eq. (25).

Figure 23 shows two sets of observables $\mathbb{E}$ each calculated using a dilution factor by sampling the ratio $\alpha_B/\alpha_T$ from a Gaussian, as discussed above. As expected, the mean value of the difference $\Delta\mathbb{E}$ is zero. The upper estimate of the systematic uncertainty associated with the dilution factor is estimated to be $\sigma^{sys}_{Empty\ target} = 0.020$.

## 3.7 Systematic effect of fiducial cuts

Fiducial cuts aim in removing regions of the CLAS detector where the acceptance varies rapidly. These correspond to regions around the torus magnets, at the end of each sector. As we do no see any large systematic effects of fiducial cuts we decided not to remove these regions in our nominal determination of $\mathbb{E}$. To study the effect the inclusion of these cut might have on our determined observable, a 6-degree cuts in the azimuthal angle of both kaon and pion was applied around each sector (i.e. sector 1 cut includes particles with $-27° < \phi < 27°$, sector 2 $33° < \phi < 87°$, ...).
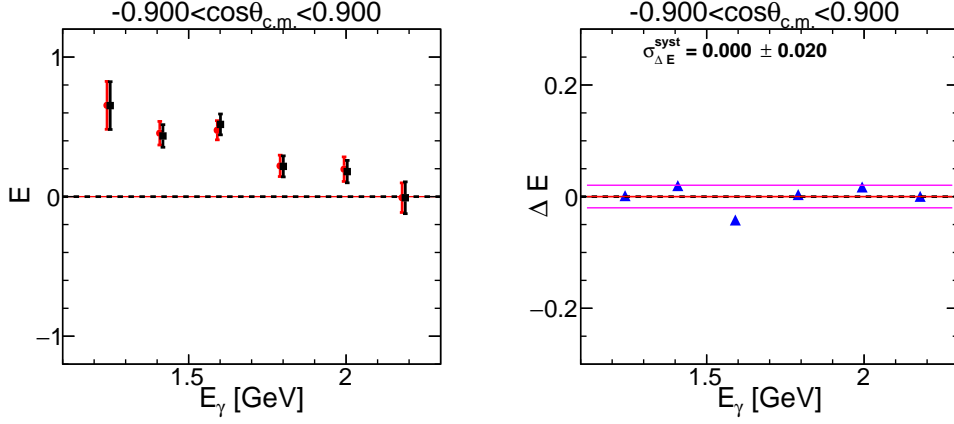
Figure 23: Systematic study associated with the statistical uncertainty of empty target subtraction. Left panel shows the determined observables for an integrated $\cos\theta_{c.m.}$ bin using $\alpha_B/\alpha_T$ values sampled from a Gaussian with mean $(\alpha_B/\alpha_T)_{calc}$ and standard deviation equal to double the statistical uncertainty of the asymmetry and the right panel shows the difference $\Delta\mathbb{E}$.

Figure 24 shows the observable $\mathbb{E}$ determined using no fiducial cuts and 6degree wide fiducial cuts (in the azimuthal angle only). From this, an upper
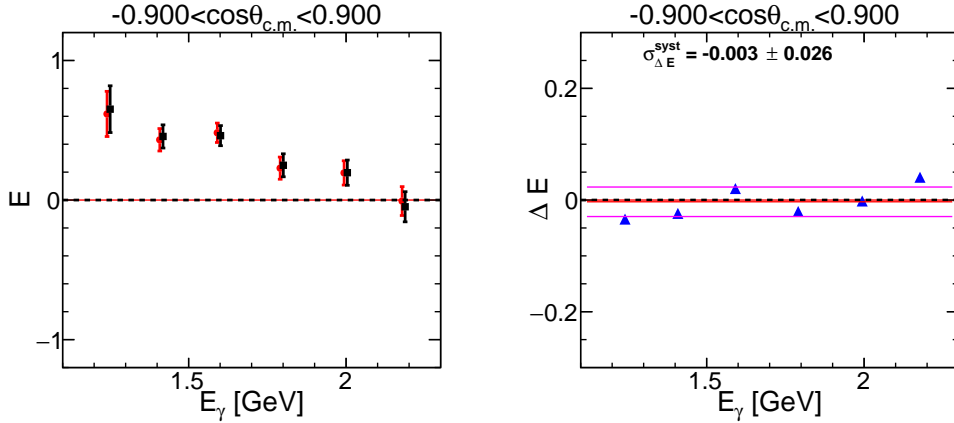


Figure 24: Systematic study associated with fiducial cuts. Left panel shows the determined observables for an integrated $\cos\theta_{c.m.}$ bin determined using fiducial cuts and no cuts applied. The right panel shows the difference $\Delta\mathbb{E}$.

value of the systematic uncertainty associated with fiducial cuts was esti-

mated at $\sigma^{sys}_{Fid.\ cut} = 0.029$.

## 3.8  Systematic effect of target and photon polarization

As the target and photon polarization enter in the determination of $\mathbb{E}$ as a scale of the asymmetry, their uncertainties can be directly propagated to $\mathbb{E}$. Specifically, the total target polarization uncertainty was determined to be $\sigma_{TarPol}/P_{targ} = 6\%$ (see Ref. [2] for a detailed discussion on the determination of this). This uncertainty is directly propagated such that the systematic uncertainty on $\mathbb{E}$ due to the target polarization uncertainty is $\sigma^{sys}_{TarPol}/\mathbb{E} = 6\%$.

The same procedure follows for the uncertainty related to the photon polarization. This was estimated to be $\sigma_{P_\circ}/P_\circ < 3.4\%$ [2], which is directly propagated to an upper estimate of the systematic uncertainty on $\mathbb{E}$: $\sigma^{sys}_{P_\circ}/\mathbb{E} = 3\%$[3]. As our method for determining the observable was based on an event-by-event analysis, this uncertainty propagation was tested by changing the value of polarization for each event by 3%. Figure 25 shows the results by comparing the two values of $\mathbb{E}$ with each event having the calculated $P^i_\circ$ and $P^i_\circ * 1.03$. It is evident that the difference depends on the value of $\mathbb{E}$ and in fact the value of $\sigma^{sys}_{P_\circ}/\mathbb{E} = 3\%$. This indicates that the propagation of the uncertainty of photon polarization in our event-by-event analysis is consistent with the binned technique.

---

[3]This was determined by propagating the uncertainty of the electron polarization from the M øller measurements (which is purely statistical as the systematic error for the Hall-B polarimeter is about $\pm0.03\%$). The statistical uncertainty of $P_e$ is of the order of 2%, however the polarimeter foils which were inspected around 2010 showed some radiation damage and that they were not completely planar. The effect on the electron polarization due to these effects was estimated at about 2%, making the overall uncertainty of the electron polarization $\sim 3.4\%$. As the uncertainty of the ratio $E_\gamma/E_e$ is much smaller, it is safe to assume that the ratio $E_\gamma/E_e$ is precisely known. Therefore, the uncertainty of the degree of photon polarization is directly propagated from the uncertainty of electron polarization.
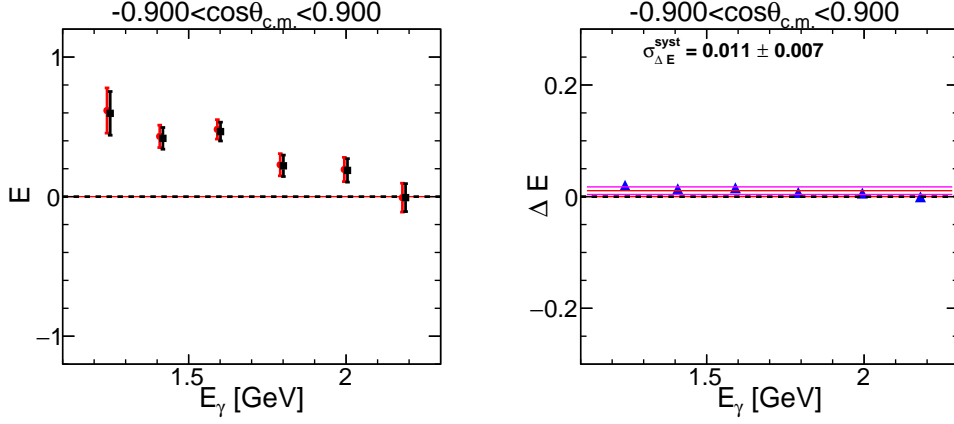
Figure 25: Systematic study associated with the degree of photon polarization. Left panel shows the determined observables for an integrated $\cos\theta_{c.m.}$ bin for two event-by-event values of $P_\circ$ ($P_\circ^i$ and $P_\circ^i * 1.03$) and the right panel shows the difference $\Delta\mathbb{E}$.

## 3.9 Systematic effect of method for determination of $\mathbb{E}$

The two main methods employed for the determination of $\mathbb{E}$ yield consistent results with RMS values below 0.005, and thus we consider our method to produce reliable results.

## 3.10 Summary of systematic uncertainties

Table 3.10 summarizes the systematic uncertainties estimated for this analysis. The values quoted represent the upper limits of the systematics.

34

| Source | $\sigma^{sys}$ |
|---|---|
| Kaon PID | 0.013 |
| Pion PID | 0.024 |
| Particle Misidentification | 0.005 |
| $\Lambda/\Sigma^0$ separation | 0.055 |
| Kaon decayed events | 0.048 |
| $\Sigma^*$ background subtraction | 0.047 |
| Empty target subtraction | 0.020 |
| Fiducial cuts | 0.029 |
| Method of extraction observable | 0.005 |
| **Total Absolute Systematic** | **0.10** |
| Target Polarization | 6% |
| Photon Polarization | 3.4% |
| **Total Relative Systematic** | **6.9%** |

Table 4: Summary of systematic uncertainties related to the determination of $\mathbb{E}$

# 4  Results

Our data were binned in $\cos\theta_{K+}^{c.m.}$ and $E_\gamma$. Specifically, we used 6 photon-energy bins 200 MeV wide between 1.1 and 2.3 GeV. Six angular bins were employed with different widths in an attempt to keep the statistical uncertainty constant between the bins. Figure 26 shows the $\cos\theta^{c.m}$ as a function of $E_\gamma$ for all available data. The right panel shows indicates the statistics for each kinematic bin.
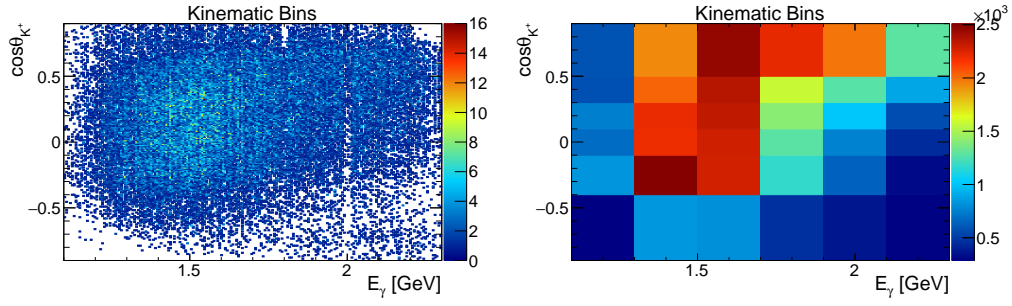


Figure 26: Left: $\cos\theta^{c.m}$ as a function of $E_\gamma$ for all available data; Right: binning used for the presentation of our determined observable.

Figure 27 shows the angular dependence of the determined observable $\mathbb{E}$ for the six photon-energy bins. The uncertainties shown are only statistical. The different points shows the two different methods for determining $\mathbb{E}$.

Table 4 shows the results for the extracted observables $\mathbb{E}$ along with the binning and determined uncertainties.

Figure 27: Angular dependence of the determined observable $\mathbb{E}$ for the six photon-energy bins. The uncertainties shown are only statistical.

37

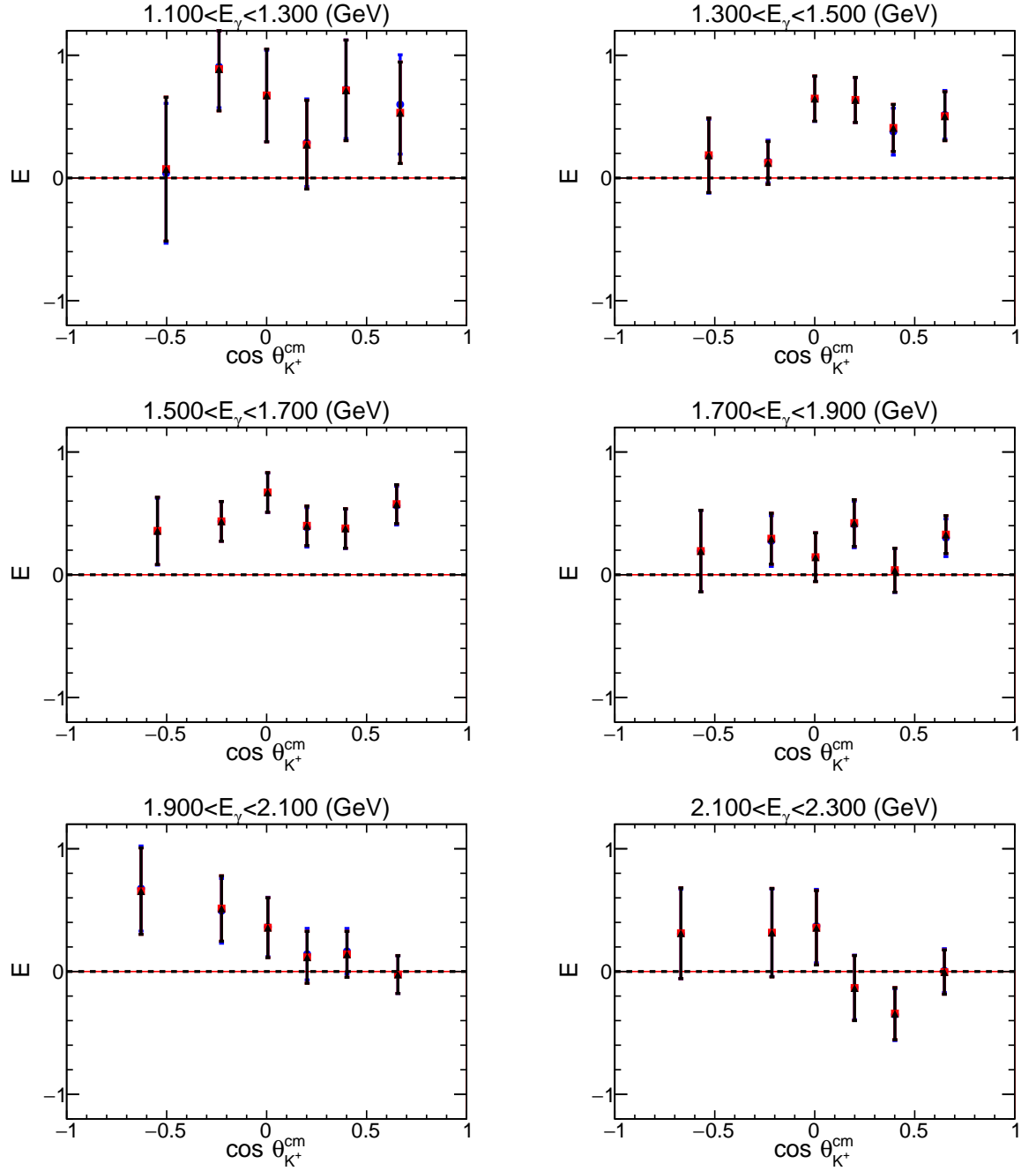| $E_\gamma^{low}$ | $E_\gamma^{high}$ | $E_\gamma^{ave}$ | $\cos\theta_{K^+-c.m.}^{low}$ | $\cos\theta_{K^+-c.m.}^{high}$ | $\cos\theta_{K^+-c.m.}^{ave}$ | $\mathbb{E}$ | $\sigma_\mathbb{E}^{stat}$ | $\sigma_\mathbb{E}^{sys}$ | $\sigma_\mathbb{E}^{tot}$ |
|---|---|---|---|---|---|---|---|---|---|
| 1.100 | 1.300 | 1.244 | -0.900 | -0.400 | -0.503 | 0.038 | 0.570 | 0.100 | 0.578 |
| 1.100 | 1.300 | 1.239 | -0.400 | -0.100 | -0.238 | 0.906 | 0.334 | 0.118 | 0.354 |
| 1.100 | 1.300 | 1.242 | -0.100 | 0.100 | 0.000 | 0.668 | 0.372 | 0.110 | 0.388 |
| 1.100 | 1.300 | 1.241 | 0.100 | 0.300 | 0.201 | 0.287 | 0.357 | 0.102 | 0.371 |
| 1.100 | 1.300 | 1.246 | 0.300 | 0.500 | 0.397 | 0.723 | 0.401 | 0.112 | 0.417 |
| 1.100 | 1.300 | 1.236 | 0.500 | 0.900 | 0.668 | 0.599 | 0.405 | 0.108 | 0.419 |
| 1.300 | 1.500 | 1.406 | -0.900 | -0.400 | -0.530 | 0.178 | 0.301 | 0.101 | 0.317 |
| 1.300 | 1.500 | 1.406 | -0.400 | -0.100 | -0.233 | 0.135 | 0.174 | 0.100 | 0.201 |
| 1.300 | 1.500 | 1.409 | -0.100 | 0.100 | 0.000 | 0.644 | 0.183 | 0.109 | 0.213 |
| 1.300 | 1.500 | 1.410 | 0.100 | 0.300 | 0.203 | 0.634 | 0.183 | 0.109 | 0.213 |
| 1.300 | 1.500 | 1.410 | 0.300 | 0.500 | 0.393 | 0.378 | 0.191 | 0.103 | 0.217 |
| 1.300 | 1.500 | 1.409 | 0.500 | 0.900 | 0.651 | 0.515 | 0.198 | 0.106 | 0.225 |
| 1.500 | 1.700 | 1.588 | -0.900 | -0.400 | -0.546 | 0.351 | 0.272 | 0.103 | 0.291 |
| 1.500 | 1.700 | 1.589 | -0.400 | -0.100 | -0.226 | 0.434 | 0.161 | 0.104 | 0.192 |
| 1.500 | 1.700 | 1.589 | -0.100 | 0.100 | 0.005 | 0.666 | 0.161 | 0.110 | 0.195 |
| 1.500 | 1.700 | 1.590 | 0.100 | 0.300 | 0.201 | 0.386 | 0.160 | 0.103 | 0.191 |
| 1.500 | 1.700 | 1.591 | 0.300 | 0.500 | 0.394 | 0.374 | 0.160 | 0.103 | 0.191 |
| 1.500 | 1.700 | 1.597 | 0.500 | 0.900 | 0.650 | 0.563 | 0.158 | 0.107 | 0.191 |
| 1.700 | 1.900 | 1.792 | -0.900 | -0.400 | -0.570 | 0.194 | 0.329 | 0.101 | 0.344 |
| 1.700 | 1.900 | 1.785 | -0.400 | -0.100 | -0.217 | 0.275 | 0.207 | 0.102 | 0.230 |
| 1.700 | 1.900 | 1.787 | -0.100 | 0.100 | 0.004 | 0.144 | 0.198 | 0.100 | 0.222 |
| 1.700 | 1.900 | 1.791 | 0.100 | 0.300 | 0.198 | 0.409 | 0.189 | 0.104 | 0.216 |
| 1.700 | 1.900 | 1.792 | 0.300 | 0.500 | 0.401 | 0.034 | 0.178 | 0.100 | 0.204 |
| 1.700 | 1.900 | 1.794 | 0.500 | 0.900 | 0.656 | 0.301 | 0.153 | 0.102 | 0.184 |
| 1.900 | 2.100 | 1.995 | -0.900 | -0.400 | -0.628 | 0.676 | 0.347 | 0.110 | 0.364 |
| 1.900 | 2.100 | 1.990 | -0.400 | -0.100 | -0.226 | 0.494 | 0.264 | 0.106 | 0.284 |
| 1.900 | 2.100 | 1.992 | -0.100 | 0.100 | 0.006 | 0.363 | 0.242 | 0.103 | 0.263 |
| 1.900 | 2.100 | 1.994 | 0.100 | 0.300 | 0.203 | 0.142 | 0.210 | 0.100 | 0.233 |
| 1.900 | 2.100 | 1.994 | 0.300 | 0.500 | 0.402 | 0.165 | 0.186 | 0.101 | 0.212 |
| 1.900 | 2.100 | 1.995 | 0.500 | 0.900 | 0.657 | -0.026 | 0.153 | 0.100 | 0.183 |
| 2.100 | 2.300 | 2.180 | -0.900 | -0.400 | -0.669 | 0.307 | 0.365 | 0.102 | 0.379 |
| 2.100 | 2.300 | 2.179 | -0.400 | -0.100 | -0.214 | 0.315 | 0.356 | 0.102 | 0.370 |
| 2.100 | 2.300 | 2.178 | -0.100 | 0.100 | 0.008 | 0.370 | 0.299 | 0.103 | 0.317 |
| 2.100 | 2.300 | 2.177 | 0.100 | 0.300 | 0.199 | -0.129 | 0.263 | 0.100 | 0.281 |
| 2.100 | 2.300 | 2.180 | 0.300 | 0.500 | 0.401 | -0.352 | 0.211 | 0.103 | 0.235 |
| 2.100 | 2.300 | 2.176 | 0.500 | 0.900 | 0.649 | 0.007 | 0.179 | 0.100 | 0.205 |

Table 5: Results for observable $\mathbb{E}$

# 5   Discussion and Conclusion

The results were compared with the latest available reaction PWA for $\gamma n \rightarrow K^+ \Sigma^-$ from MAID  and Bonn-Gatchina  These give divergent predictions for this observable for certain regions of photon energies and kaon angles. The KaonMAID tends to give better agreement in the lower photon energy ranges while at higher photon energies, both KaonMAID and Bonn-Gatchina describe our available data with the same degree of success. Figure 28 and Fig. 29 shows the Kaon MAID predictions from 2000  and 2017  respectively. Figure 30 shows the Bonn-Gatchina predictions  Red dashed lines show predictions for the lower-edge of the photon-energy bin, magenta shows the predictions calculated at the upper-edge of the photon-energy bin, and the blue lines show the predictions at the average photon-energy bins.   Figure 31 shows the determined observable compared with all three available theoretical predictions at the average photon-energy bin.

This new experimental results on the double polarization observable $\mathbb{E}$ will provide valuable constraints on these models and the nucleon resonances that contribute at these photon energies.
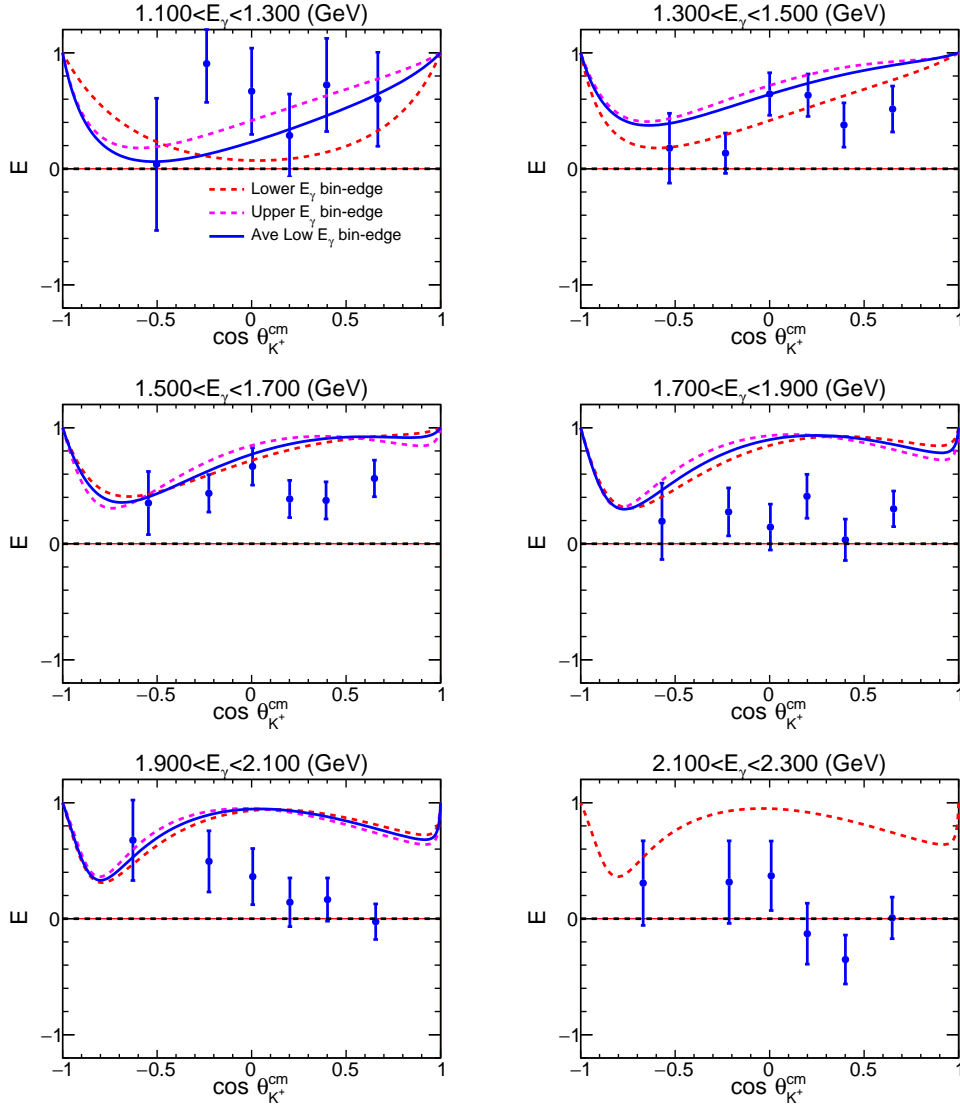
Figure 28: Angular dependence of the determined observable $\mathbb{E}$ for the six photon-energy bins compared with the Kaon MAID 2000 predictions.
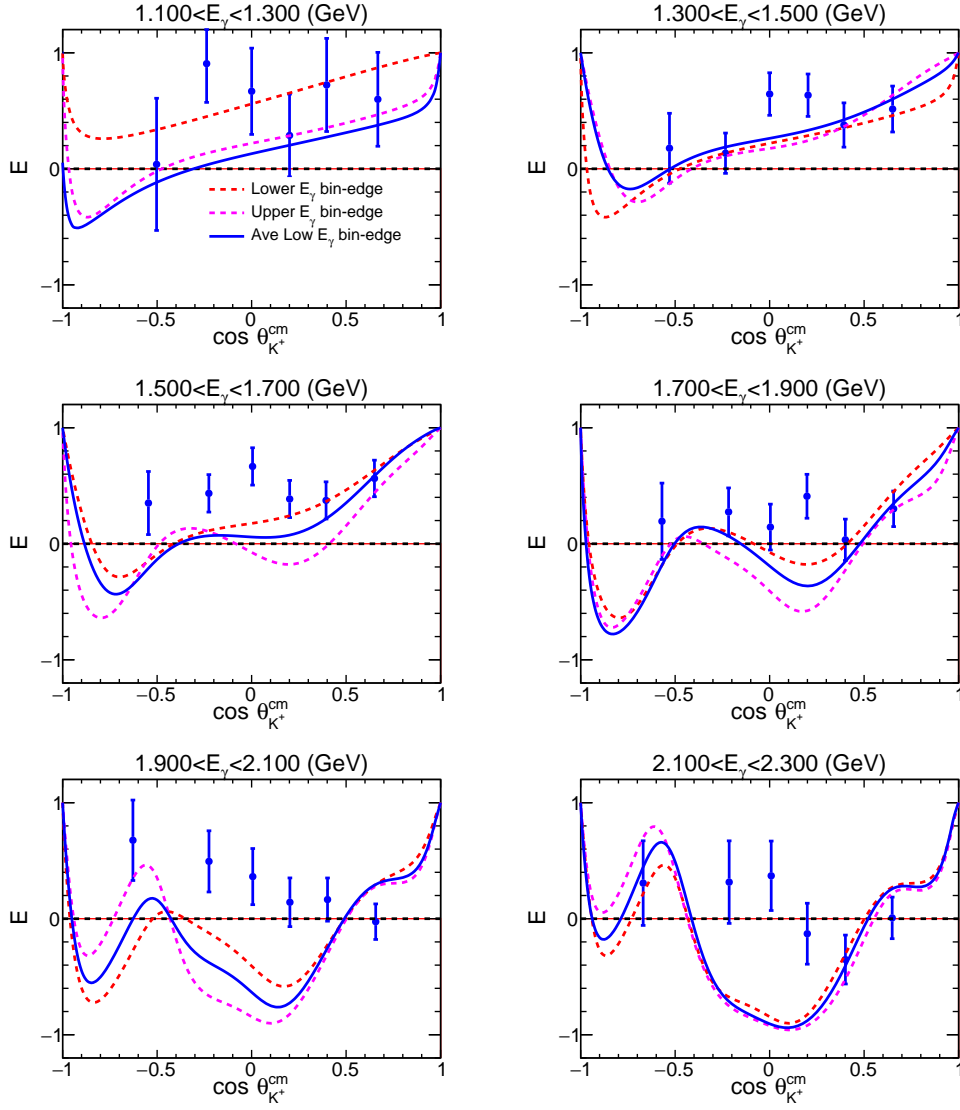
Figure 29: Angular dependence of the determined observable $\mathbb{E}$ for the six photon-energy bins compared with the Kaon MAID 2017 predictions.
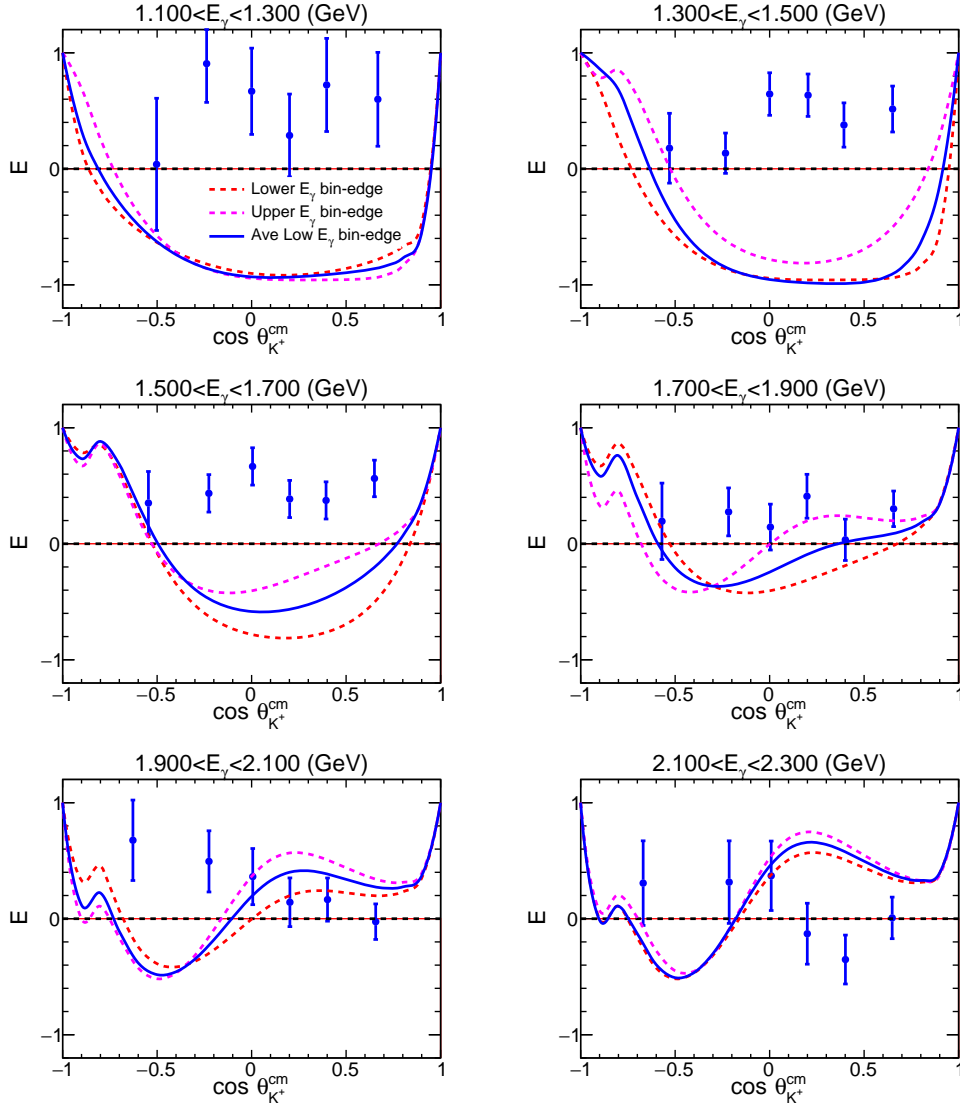
Figure 30: Angular dependence of the determined observable $\mathbb{E}$ for the six photon-energy bins compared with the Bonn-Gatchina predictions.
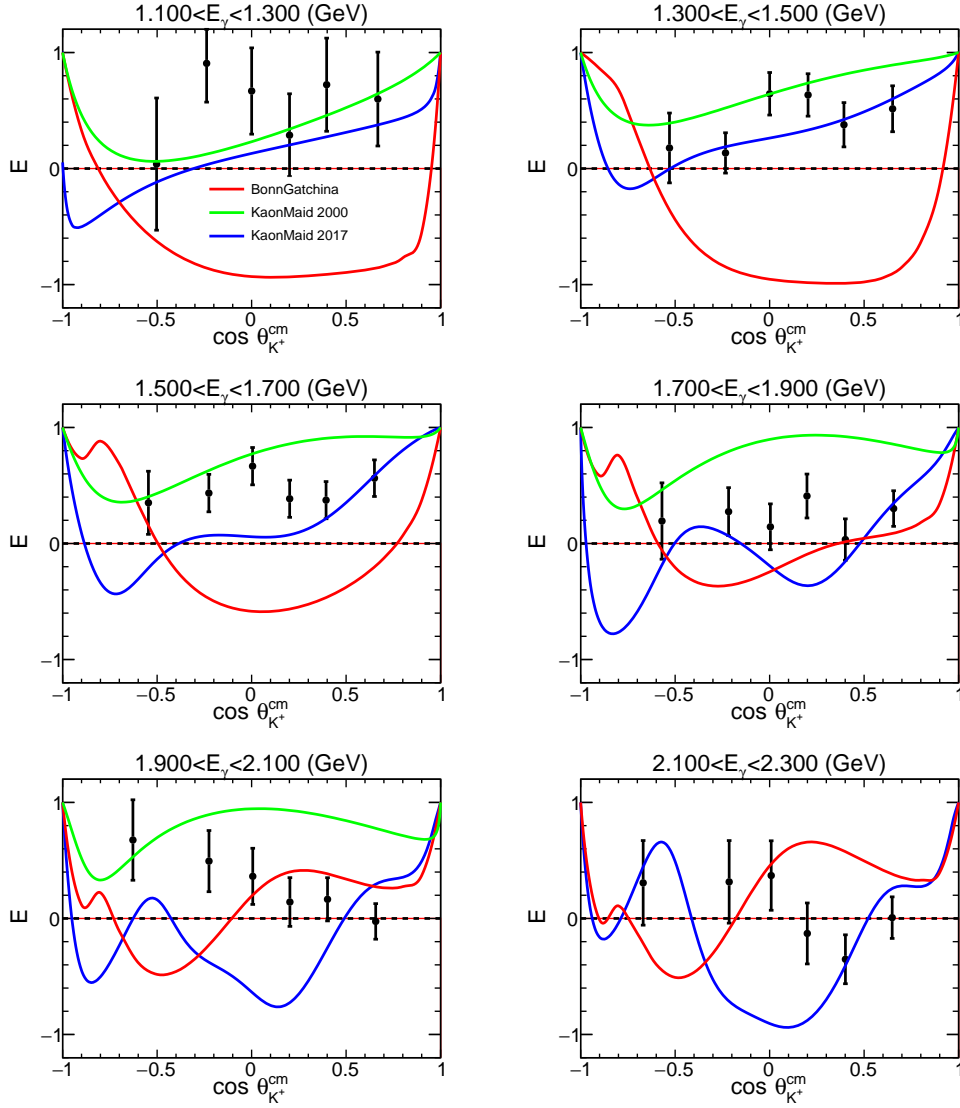
Figure 31: Angular dependence of the determined observable $\mathbb{E}$ for the six photon-energy bins compared with the Kaon MAID200, and 2017, as well as Bonn-Gatchina predictions.

[1] I. Barker and A. Donnachie, "Complete Experiments in Pseudoscalar Photoproduction", *Nucl. Phys. B*, vol. 95, pp. 347–356, 1975.

[2] D. Ho, P. Peng, T. Kageya, F. Klein, A. Sandorfi, and R. Schumacher, "E asymmetry for $\vec{\gamma}\vec{n} \to \pi^- p$ from g14 (HDice) data", *CLAS Analysis Note 2016-104*, 2016.

[3] X. Wei *et. al.*, "HDice, the polarized Solid HD target in the Frozen Spin Mode for Experiments with CLAS", *J. Phys. Conf. Ser.*, vol. 400, p. 052 042, 2012.

[4] *CLAS HDice target*, https://www.jlab.org/Hall-B/HDIce/.

[5] *See*, http://clasweb.jlab.org/rungroups/g14/monitor/monitorwrapper.html and http://clasweb.jlab.org/rungroups/g14/anamon/monitorwrapper.html.

[6] E. Pasyul, "The CLAS Eloss Package", *CLAS-NOTE 2003-017*, 2003.

[7] H. Olsen and L. Maximon, "Photon and Electron Polarization in High-Energy Bremsstrahlung and Pair Production with Screening", *Phys. Rev*, vol. 114, p. 887, 1959.

[8] *TMinuit Class Reference*, https://root.cern.ch/doc/v610/classTMinuit.html.

[9] J. Fliming, *First Measurement of the* $\mathbb{E}$ *Double-polarization Observable for the* $\gamma n \to K^+ \Sigma^-$ *with CLAS*, https://www.jlab.org/Hall-B/general/thesis/Fleming_thesis.pdf.